9-2019

Evaluation of External Surface Modification Techniques to Enhance Pool Boiling of Dielectric Fluids

Farhan Mody
fdm8746@rit.edu

R.I.T

Evaluation of External Surface Modification Techniques to Enhance Pool Boiling of Dielectric Fluids

by

Farhan Mody

A Thesis Submitted in Partial Fulfilment of the Requirements for the

Degree of Master of Science in Mechanical Engineering

Thermal Analysis, Microfluidics and Fuel Cell Lab,

Department of Mechanical Engineering

Kate Gleason College of Engineering

ROCHESTER INSTITUTE OF TECHNOLOGY

Rochester, New York

September 2019

Evaluation of External Surface Modification Techniques to Enhance Pool Boiling of Dielectrics Fluids

By: Farhan Mody

A Thesis Submitted in Partial Fulfilment of the Requirements for the Degree of Master of Science in Mechanical Engineering

Department of Mechanical Engineering

Kate Gleason College of Engineering

Rochester Institute of Technology

Approved by:

Dr. Satish Kandlikar

Thesis Advisor *Date*

Department of Mechanical Engineering

Dr. Michael Schertzer

Thesis Committee Member *Date*

Department of Mechanical Engineering

Dr. Mario Gomes

Thesis Committee Member *Date*

Department of Mechanical Engineering

Dr. Michael Schrlau

Department Representative, Thesis Committee Member *Date*

Department of Mechanical Engineering

Abstract

The miniaturization trend of transistors and increase in packing density of electronic devices has resulted in high heat flux generation, which has created a need for efficient heat removal systems. The present research is an experimental study of pool boiling using plain copper chip and microchannel chip with boiling surface of 34.5mm x 32mm. Three dielectric fluids, Perfluoro-2-methylpentane (PP1), perfluoro-methyl-cyclopentane (PP1C), and fluorocarbon (FC-87) were used in a closed loop pool boiling system to determine their performance at atmospheric pressure. The pool boiling results have been compared with literature for a boiling surface of 10 mm x 10 mm to study the effect of heater size.

To improve the performance of the pool boiling system, we desire high critical heat flux and low surface temperatures. In the current study, we introduced two external structures fitted on the test surfaces for regulating the flow of vapor through specific structures and generating independent liquid-vapor pathways without any deposition and/or chemical surface modifications of the test surface. Firstly, an array of hollow conical structures (HCS) called volcano manifold are printed using additive manufacturing technique. A critical heat flux (CHF) of 28.1 W/cm², 38.3 W/cm² and 32.5 W/cm² was achieved for volcano manifold with plain copper chip using PP1, PP1C and FC87 respectively giving 19%, 33% and 6.5% enhancement in CHF respectively as compared to a plain chip without volcano manifold. Secondly, dual taper manifold having taper angle of 15° is printed using a stereolithography (SLA) additive manufacturing technique. Plain chip with dual taper manifold gave the CHF of 25.6 W/cm², 31.7 W/cm² and 32.3 W/cm² for PP1, PP1C and FC-87, respectively. These results indicate a deterioration in CHF caused by vapor constriction. In addition, the heater size effect was studied by comparing the pool boiling performance of a plain copper boiling surface of 34.5 mm x 32 mm (Large heater) with 10 mm x 10 mm (Small heater) from published literature for all three refrigerants. It was noted that 31%, 66% and 104% increment in maximum heat

transfer coefficient was obtained for PP1, PP1C and FC-87 respectively with larger heater over smaller heater at CHF. The geometrical parameters of the enhancement structures were based on published results for water. The results show that the external surface modification techniques require further geometrical parameter optimization as the current designs based on water performance caused vapor constriction effects that caused performance deterioration for dielectric fluids.

Acknowledgements

I would like to sincerely express my gratitude to Dr. Satish Kandlikar for giving me this opportunity to work at the Thermal Analysis, Microfluidics and Fuel Cell Laboratory. This work would not have been possible without your support and guidance. I would also like to thank my committee members Dr. Satish Kandlikar, Dr. Michael Schertzer, Dr. Mario Gomes and Dr. Michael Schrlau for their support in evaluating my thesis. Thank you to Craig Arnold and Rob Kraynik from RIT's Machine shop for their efforts in fabrication of the test setup and all the TAMFL members for their laughs, help and support.

Finally, I would like to thank my family for giving me this opportunity for pursuing master's degree and for their support and encouragement. I would also like to thank my girlfriend Priya for believing in me and supporting me through thick and thin.

Table of Contents

Abstract ---------- **3**

Acknowledgements ---------- **5**

List of Figures ---------- **9**

List of Tables ---------- **12**

Abbreviations ---------- **13**

1. Introduction ---------- **14**

1.1 Pool Boiling Heat Transfer ---------- 15

1.1.1 Free/Natural Convection Boiling ---------- 16

1.1.2 Nucleate Boiling ---------- 17

1.1.3 Transition Boiling ---------- 17

1.1.4 Film Boiling ---------- 17

1.2 Additive Manufacturing ---------- 18

1.2.1 Stereolithography (SLA) ---------- 19

1.2.2 Fused Deposition Modelling (FDM) ---------- 20

2. Literature Review ---------- **21**

2.1 Pool Boiling over Open Microchannel ---------- 21

2.2 Pool Boiling using Refrigerants ---------- 23

2.3 Separate Liquid Vapor Pathways for Boiling Enhancement ---------- 26

2.4 Pool Boiling of Scaled Heater ---------- 29

2.5 Scope of Work ---------- 31

3. Experimental Setup ---------- 32

3.1 Test Section---------- 32

3.2 Volcano Manifold ---------- 34

3.3 Dual Taper Manifold ---------- 35

3.4 Pool Boiling Setup---------- 37

3.5 Experimental Procedure & Setup Validation ---------- 39

4. Data Acquisition ---------- 41

5. Uncertainty Analysis ---------- 43

6. Results & Discussions ---------- 45

6.1 Plain Copper Chip ---------- 45

6.2 Microchannel Chip---------- 47

6.3. Volcano Manifold---------- 49

6.3.1 Plain Copper Chip with the Volcano Manifold ---------- 51

6.3.2 Microchannel chip with volcano manifold ---------- 54

6.4 Dual Taper Manifold ---------- 55

6.4.1 Plain copper chip with dual taper manifold---------- 55

6.4.2 Microchannel chip with dual taper manifold ---------- 58

6.5 Comparison of Larger Heater with Small Heater---------- 60

7. Conclusions---------- 63

8. Recommendations for Future Work---------- 65

9. References ---------- 67

Appendix---------- 71

Validation of Fourier's Law of 1-D conduction ---------- 71

Heat loss study of the heating chip ---------- 73

List of Figures

Figure 1. Pool boiling curve. ---------- 16

Figure 2. Schematic of 3D printing process. ---------- 18

Figure 3. Stereolithography additive manufacturing technique.---------- 19

Figure 4. Fused deposition additive manufacturing technique.---------- 20

Figure 5. Microchannel surface [9]. ---------- 21

Figure 6. Bubble dynamics on a microchannel surface in pool boiling [10].---------- 22

Figure 7. Heat transfer coefficient for tested chips [11]. ---------- 22

Figure 8. a) Pool boiling curve and b) HTC for tested refrigerants [13]. ---------- 23

Figure 9. Pool boiling curve for tested chips with FC-87 at atmospheric pressure [14]. ----- 24

Figure 10. Test heater [15]. ---------- 25

Figure 11. a) Sintered fin tops and b) Sintered channels [16].---------- 26

Figure 12. a)Bi-conductive fabricated surfaces, (b-d) SEM image of epoxy divisions in copper substrate, e) high speed image of bi-conductive surface [17].---------- 27

Figure 13. a) Schematic of separate liquid vapor pathway on NRFC configuration, b) picture of bubbles nucleating from nucleation region and the feeder channels, c) Top view of NRFC-3 chip [18]. ---------- 28

Figure 14 Pathway a) liquid entering from side holes and vapor exits from top hole, b) liquid entering from top and vapor exits from the side holes [19] ---------- 29

Figure 15. Effect of heater size on pool boiling curve of pure water [20].---------- 30

Figure 16. Pool boiling curve for 1-cm², 4-cm² and 25-cm² heater surface [22]. ---------- 31

Figure 17. Test section a) Top view, b) Front view. ---------- 32

Figure 18. Schematic of heater section.---------- 33

Figure 19. a) Schematic heater assembly, b) Actual Image of heater assembly.---------- 33

Figure 20. Volcano manifold, a) Top view, b) Side view. ---------- 34
Figure 21. Heater assembly with volcano manifold. ---------- 35
Figure 22. Dual taper manifold, a) Top view, b) Front view, and c) 3D Bottom view. ------- 36
Figure 23. Heater assembly with dual taper manifold, a) Design and b) Actual image. ------ 37
Figure 24. Schematic pool boiling setup. ---------- 38
Figure 25. Pool boiling setup. ---------- 38
Figure 26. 1-D Conduction in copper block. ---------- 41
Figure 27. Variation in uncertainty with increasing heat flux for tested refrigerants with plain chip. ---------- 44
Figure 28. Temperature variation over heater block for various heat fluxes. ---------- 44
Figure 29. (a) Pool boiling curve and (b) HTC for tested refrigerants with plain copper chip. ---------- 46
Figure 30. High-speed images of bubbles nucleation over plain copper chip with PP1 at atmospheric pressure at 5 W/cm², 13 W/cm², 19 W/cm², 24 W/cm² and CHF. ---------- 47
Figure 31. (a) Pool boiling curve and (b) HTC for tested refrigerants with microchannel chip. ---------- 48
Figure 32. Volcano manifold, (a) No rewetting holes and (b) With rewetting holes. --------- 49
Figure 33. (a) Pool boiling curve and (b) HTC plain chip with PP1C at atmospheric pressure using volcano manifolds with rewetting holes 0.635mm, 1mm and 1.5mm. ---------- 51
Figure 34. (a) Pool boiling curve and (b) HTC for tested refrigerants with plain chip and volcano manifold with rewetting holes of 1 mm diameter. ---------- 52
Figure 35. Schematic representation of separate liquid and vapor fields in volcano manifold. ---------- 52
Figure 36. High-speed images of bubbles nucleation over plain chip using volcano manifold with increasing heat flux. ---------- 53

Figure 37. (a) Pool boiling curve and (b) HTC for tested refrigerants with microchannel chip and volcano manifold with rewetting holes of 1 mm diameter. ---------- 54
Figure 38. Actual image of dual taper 15°, (a) Top view and (b) Bottom view. ---------- 55
Figure 39. (a) Pool boiling curve and (b) HTC for tested refrigerants with plain chip and dual taper manifold of 15° taper angle. ---------- 56
Figure 40. Schematic representation of separate liquid and vapor fields in Dual taper 15° manifold.---------- 57
Figure 41. High-speed images of generated vapor pathway over plain chip with FC-87 at atmospheric pressure using dual taper manifold of 15° taper angle.---------- 58
Figure 42. (a) Pool boiling curve and (b) HTC for tested refrigerants with microchannel chip and dual taper manifold of 15° taper angle. ---------- 59
Figure 43. Comparison of pool boiling performance of larger heater with smaller heater for (a) the pool boiling curve and (b) HTC vs. heat flux.---------- 60
Figure 44. (a) pool boiling over larger heater at 19 W/cm² and (b) pool boiling over smaller heater at 18.5 W/cm². ---------- 61
Figure 45. Expected bubble behaviour in dual taper manifold.---------- 65
Figure 46 Temperature distribution along the heater block in ANSYS. ---------- 71
Figure 47. Schematic of heating chip.---------- 73
Figure 48. Boundary conditions. ---------- 74
Figure 49. (a) Total heat flux and (b) Temperature distribution over the heating chip in ANSYS ---------- 75

List of Tables

Table 1. Comparison of CHF enhancement for FC-87 and water [14]. 24

Table 2. HTC and enhancement factor based of plain chip at 19°C for PP1, PP1C and FC-87. 48

Table 3. Pool boiling performance of smaller and larger heater.....62

Table 4. CHF and HTC for experiments conducted on plain chip and plain chip with volcano and dual taper manifold. 62

Table 5. The temperature comparison between experimental and numerical results at T1, T2 & T3. 72

Abbreviations

Critical heat flux	CHF
Heat transfer coefficient	HTC
Hollow conical structures	HCS
Additive manufacturing	AM
Small Heater	SH
Large Heater	LH
Perfluoro-2-methylpentane	PP1
Perfluoro-methyl-cyclopentane	PP1C
Perfluoro-1,3-dimethylcycloheaxane	PP3
Perfluoro-2-methyl-3-ethylprntane	PP80
Fluorocarbon	FC-87
Stereolithography	SLA
Fused despostion modelling	FDM
High temperature polylactide	HTPLA

1. Introduction

The electronics industry has improved performance and reduced size of electronic components over the last several decades. However, this reduction in size and improved performance of electronic components have resulted in increased thermal loads. Pool boiling is an attractive option for dissipation of large qualities of heat since it utilises phase change from liquid to vapor and latent heat of vaporization of the working fluid. Thus, two-phase cooling using boiling has more advantages than using air as single-phase cooling technique. Two-phase cooling has great application in cooling of data centres, boilers, heat exchangers, powered electronics and nuclear reactors. The performance of the pool boiling system is limited by critical heat flux (CHF), where at high heat flux bubble coalescence creates a vapor blanket over the heater surface. Whereas, heat transfer coefficient (HTC) dictates how effectively heat is dissipated from the heater surface. Performance of two-phase cooling is enhanced by dissipation of a large amount of heat through the test surface while keeping surface temperature at a minimum. Researchers have incorporated different enhancement techniques over the test surface such as roughing the surface[1], microporous coatings [2], finned surfaces [3] and nano-structures [4] to improve heat transfer performance.

Additive manufacturing allows the manufacturing of complex designed components through three-dimensional models layer-by-layer at a low cost. Taking advantage of additive manufacturing for creating pool boiling structures is an unexplored field.

1.1 Pool Boiling Heat Transfer

Pool boiling is the process in which a heater surface is submerged in a pool of liquid. As the heater surface temperature rises above the saturation temperature of the liquid at a given pressure. Bubbles are formed and vapor is generated as a result of the boiling process. During this time, heating surface temperature is greater than saturation temperature of liquid and the difference in temperatures is defined as degree of wall superheat (ΔT_{sat}). Heat flux (q'') represents the amount of heat dissipated by the heating surface per unit area and is measured in W/cm^2.

The initial work conducted by Nukiyama [5] in 1934 led to the understanding of the dependence of heat flux on wall superheat. Platinum, nichrome and nickel wires were tested with water at atmospheric pressure to identify the four regimes of pool boiling curve:

1. Free/Natural convection boiling
2. Nucleate boiling
3. Transition boiling
4. Film boiling

The four regimes of pool boiling curve are shown in Figure 1 with wall superheat (ΔT_{sat}) i.e. temperature difference between the heater surface temperature and saturated liquid on X-axis and heat flux (q'') i.e. heat dissipated from the surface on Y-axis. The pool boiling curve is dependent on the properties of the heating surface and also on the liquid used.

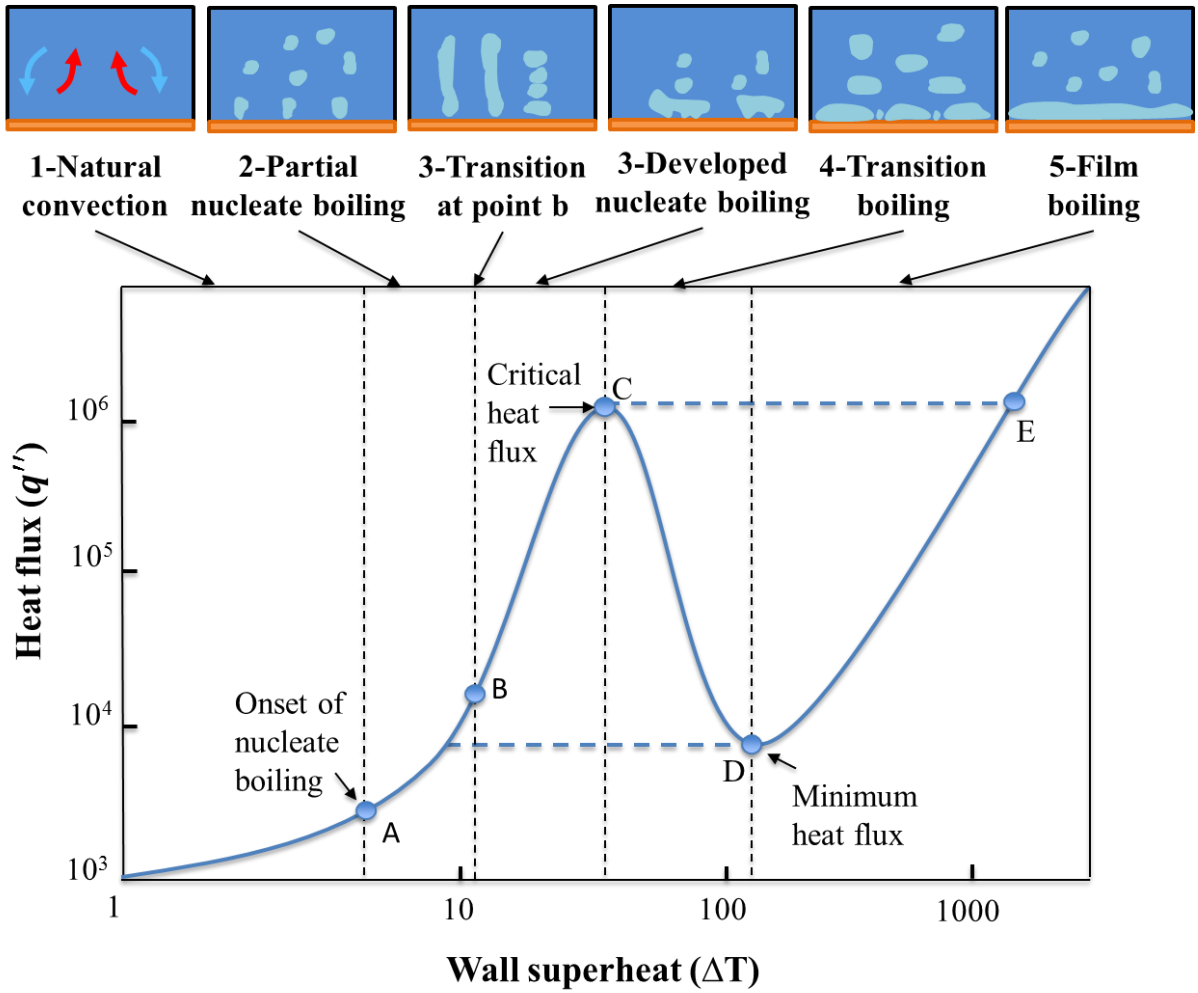

Figure 1. Pool boiling curve.

1.1.1 Free/Natural Convection Boiling

Figure 1 shows free convection boiling from origin to point 'A'. At low heat flux, the surface temperature of heating surface (T_{wall}) is greater than the saturation temperature of pool of liquid (T_{sat}). Liquid near the heating surface is at a higher temperature than the pool of liquid, thus decreasing the density of liquid close to the surface. This temperature difference results in creating a density gradient allowing the hot liquid to move upwards and cold liquid to move over the heating surface. Thus, natural convective heat is transferred from the heating surface to the pool of liquid and sustains until point 'A'.

1.1.2 Nucleate Boiling

Bubbles nucleate from cavities present on the heating surface. When bubbles first start to nucleate at point 'A' from the heating surface, it is referred to as the Onset of Nucleate Boiling (ONB). The region shown between A-B in Figure 1 is a partially developed nucleate boiling region. Isolated bubbles nucleate at various nucleation sites over the heating surface and escape into the liquid bulk, providing space for liquid to occupy over heating surface thus increasing the heat transfer coefficient (HTC). In the region B-C bubble nucleation increases and bubbles from different nucleation sites coalesce to form continuous vapor jets or columns of bubbles. Thus point 'B' is referred to as the transition from partial nucleate boiling to fully-developed nucleating boiling. Point 'C' is called Critical Heat Flux (CHF) where a sudden increase in heater surface temperature is achieved and is shown by dotted line from C-E.

1.1.3 Transition Boiling

Other boiling regimes are achieved by controlling heat flux as the input parameter. Whereas, the transition boiling region shown between C-D in Figure 1, is achieved by controlling the wall superheat. An unstable vapor film is created after the system reaches CHF. The film has low thermal conductivity, thus decreasing the heat flux and increasing ΔT.

1.1.4 Film Boiling

At point 'C' frequency of bubble nucleation increases and bubbles coalesce with neighbouring vapor columns of bubbles, forming an insulating vapor film. The vapor film prevents the liquid from coming in contact with the heater surface thereby increasing the surface temperature. At this point, heat is transferred through radiation and conduction from the heater surface to the liquid. The plot can be traced from point E-D by decreasing the heat flux, thus point 'D' is called the Leidenfrost point where heat flux is minimum (q''_{min}).

1.2 Additive Manufacturing

Additive manufacturing (AM) refers to the process of creating 3D parts from computer aided design (CAD) models by successively adding material layer by layer until a physical part is created [6]. Additive manufacturing is most commonly called "3D Printing." AM technology enables a new approach of design driven manufacturing process and allows for manufacturing of highly complex structures which could be a constraint for the conventional manufacturing process. Figure 2 shows the schematic for 3D printing process.

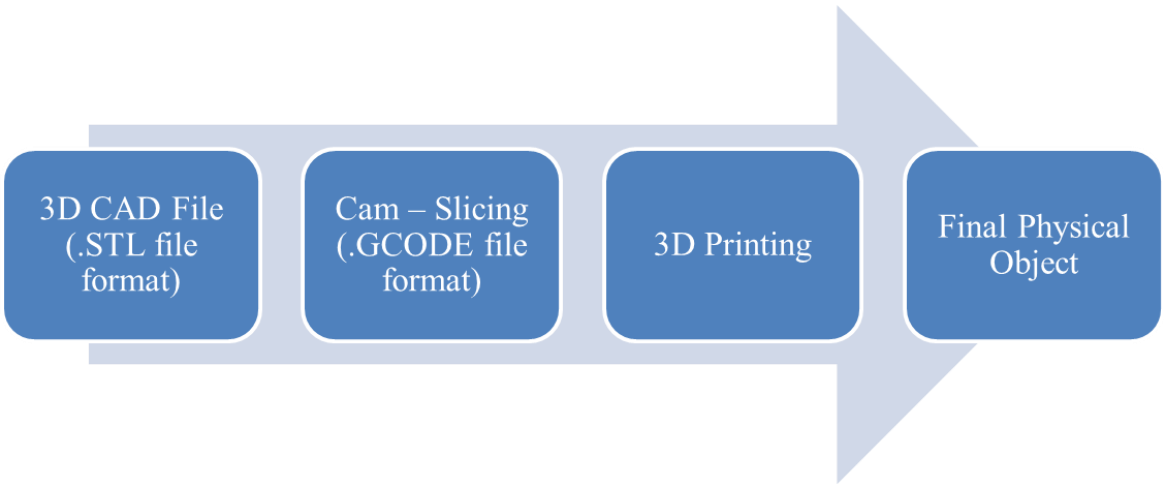

Figure 2. Schematic of 3D printing process.

Additive manufacturing is divided into following seven categories:

1. Stereolithography
2. Fused Deposition Modelling
3. Material Jetting
4. Binder Jetting
5. Sheet Lamination
6. Powder Bed Fusion
7. Directed Energy Deposition

In the current study stereolithography and fused deposition additive manufacturing have been used to fabricate the manifolds for the test section. Stereolithography (SLA) is used for its ability to print complex geometric shapes with a smooth surface finish while maintaining high precision. Form 2 3D printer works on the principle of SLA and is used in the current study. It has an accuracy of 0.050 mm and print with layer thickness with as low as 25 µm for smooth surface finish. Whereas, fused deposition (FDM) is used for its speed and is able to print 3D parts with high accuracy. FDM technique is very helpful in creating prototype design while keeping it cost friendly. Filaments used in FDM technique range from $20 to $70 per kg, making it cost friendly for initial trial prototyping of design.

1.2.1 Stereolithography (SLA)

Stereolithography is a vat photopolymerization AM method. SLA is based on the principle of using a light source-laser to cure photopolymer liquid resin into hardened plastic [7]. It was in 1986, Charles (Chuck) Hull patented the technology for stereolithography. As shown in Figure 3, the liquid resin is converted into solid 3D objects, one layer at a time.

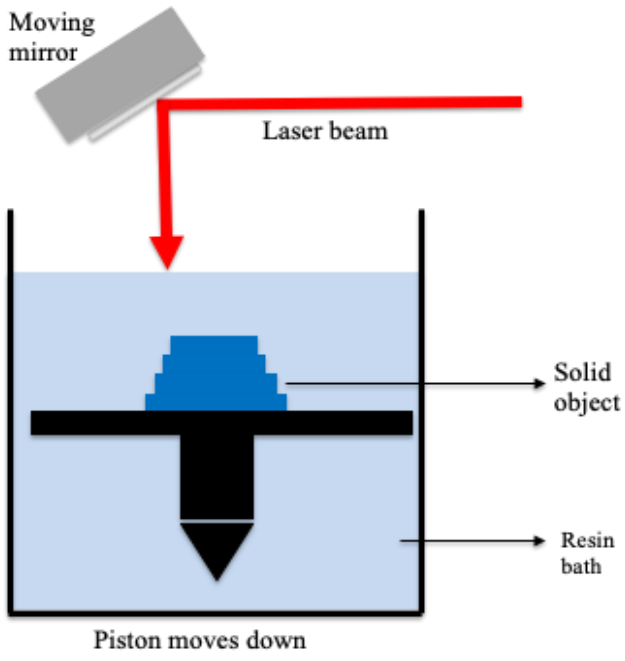

Figure 3. Stereolithography additive manufacturing technique.

The photopolymer liquid resin is first heated. Ultraviolet laser and scanning mirrors are used for printing 3D designs layer by layer. 3D objects undergo a post-curing process for removing excess resin. The print is placed in a chemical bath and then placed in an ultraviolet oven in order to make the print stronger and more stable [8].

1.2.2 Fused Deposition Modelling (FDM)

In FDM, a thin filament of plastic is heated and extruded through the nozzle onto the base, thereby printing the 3D model layer by layer on the build platform. Materials that can be used in this process are polylactide (PLA), polycarbonate (PC), acrylonitrile butadiene styrene (ABS), nylon and PC-ABS. The main advantage of this process is the broad range of materials, less time needed to manufacture and inexpensive equipment ranging from $200 - $800.

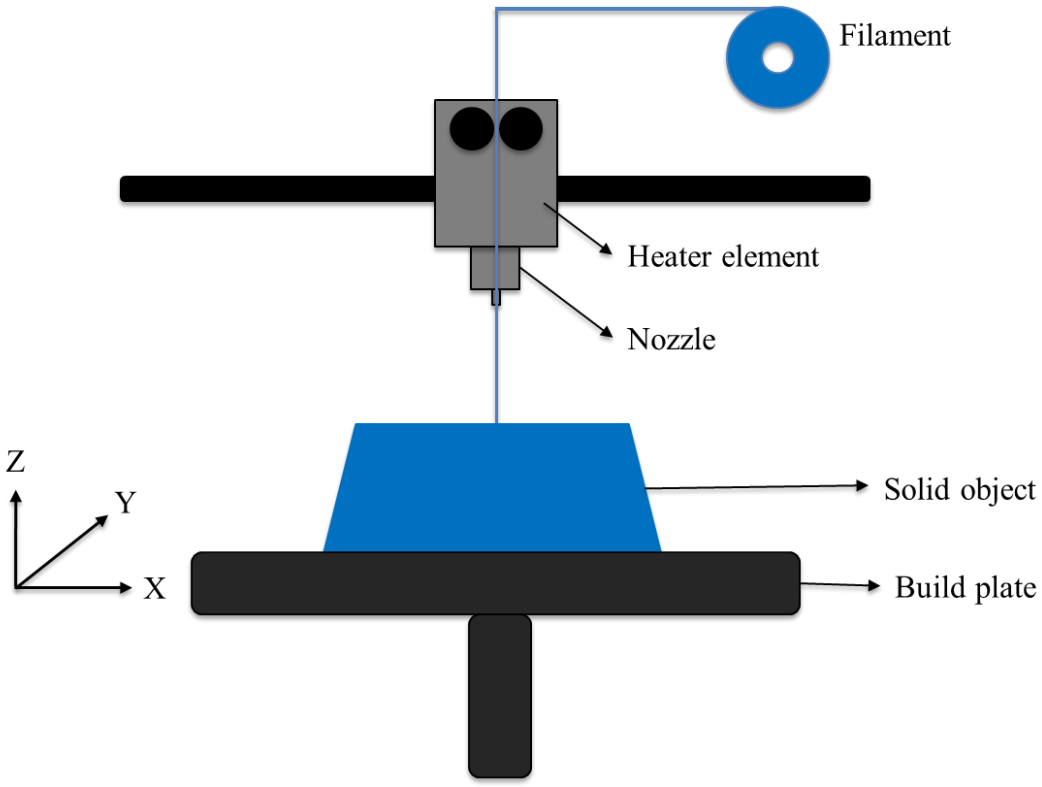

Figure 4. Fused deposition additive manufacturing technique.

2. Literature Review

2.1 Pool Boiling over Open Microchannel

Pool boiling using test surfaces with additive or subtractive modification and enhancements is an emerging field. Microchannels are widely preferred over plain surfaces for boiling due to their high surface area to volume ratio compared to a plain chip. The added amount of surface area produced in microchannels promotes an increase in heat transfer due to better convection from solid to liquid.

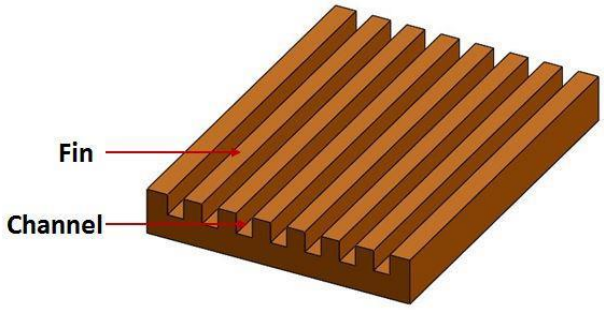

Figure 5. Microchannel surface [9].

Cooke and Kandlikar [10] studied bubble growth and heat transfer mechanism for a plain and an open microchannel silicon surface, utilizing water as the working fluid at atmospheric pressure. As shown in Figure 6 the channels are constantly in contact with the working fluid. It was observed that bubbles nucleate at the bottom of the channels and move along the channel sidewall to the fin top, where they completely grow and depart. Heat transfer coefficient (HTC) of 72.9 kW/m^{2}K at 19.5°C wall superheat was reported for microchannel chip with channel width and depth of 100 µm and 27 µm respectively [10]. They also investigated the performance of microchannels by varying the channel width (197 – 400 µm), channel depth (100 – 400 µm) and fin width (200 – 300 µm). Figure 7 shows the heat transfer performance of 10 copper chips with different microchannel parameters. It was observed that the chip with

375µm channel width, 230µm fin width and 400µm channel depth obtained a heat flux of 244 W/cm^2 and a HTC of 269 kW/m^{2}K, which was 3.7 times HTC of a plain chip [11].

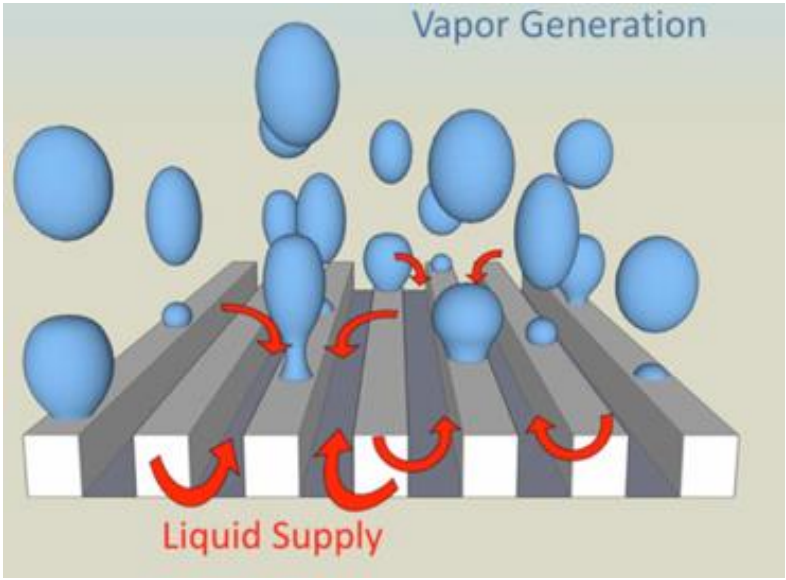

Figure 6. Bubble dynamics on a microchannel surface in pool boiling [10].

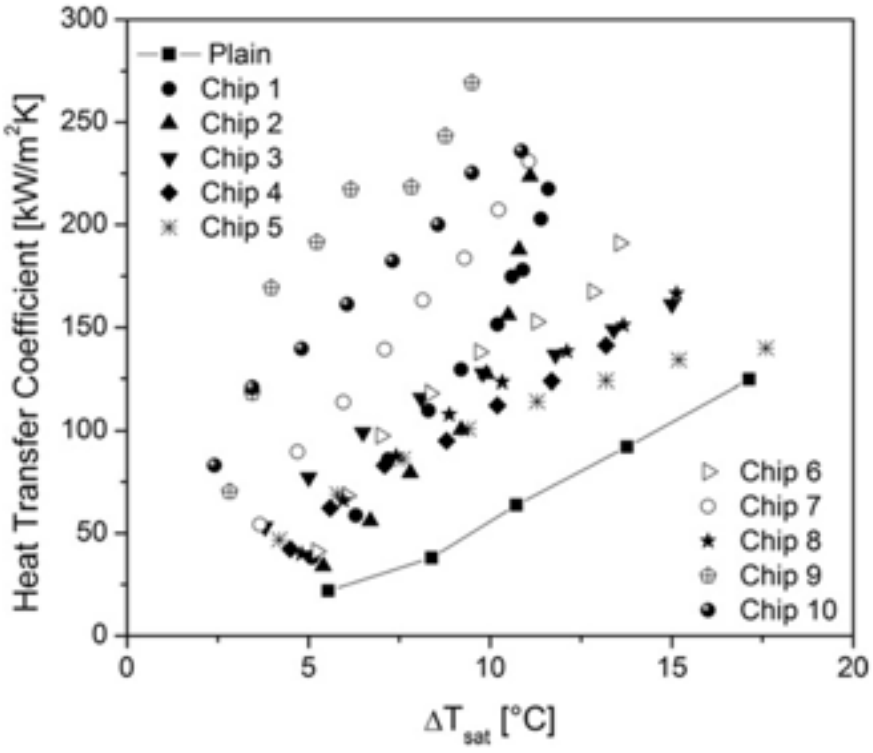

Figure 7. Heat transfer coefficient for tested chips [11].

Kalani and Kandlikar [12] used microchannel surface with ethanol at sub-atmospheric pressures for pool boiling performance. Four chips of different channel width, depth and fin width were studied at 101.3 kPa, 66.7 kPa, 33.3 kPa, and 16.7 kPa. They recorded a maximum heat flux of 1.14 MW/m^2 at 20^{o}C wall superheat at 101.3 kPa for a copper chip with channel depth and width of 470 μm and 194 μm, respectively. But the highest performing chip had channel width, fin width and channel depth of 207 μm, 193 μm and 456 μm, respectively attaining a maximum heat flux of 904 kW/m^2 with surface temperature of 85^{o}C at 33.3 kPa system pressure.

2.2 Pool Boiling using Refrigerants

Emery and Kandlikar [13] performed experiments using refrigerants PP1, PP1C, PP3, and PP80. They compared the boiling curve and HTC with experiments conducted on a polished copper chip with a 10 mm x 10 mm boiling surface. They obtained CHF of 15.6 W/cm^2, 16 W/cm^2, 13.4 W/cm^2, and 14.2 W/cm^2, for PP1, PP1C, PP3 and PP80, respectively. As shown in Figure 10 it is observed that FC-87 outperforms PP3 and PP80 in CHF. Whereas PP1 exhibits better HTC over PP1C, even after achieving similar CHF values because of low wall superheat.

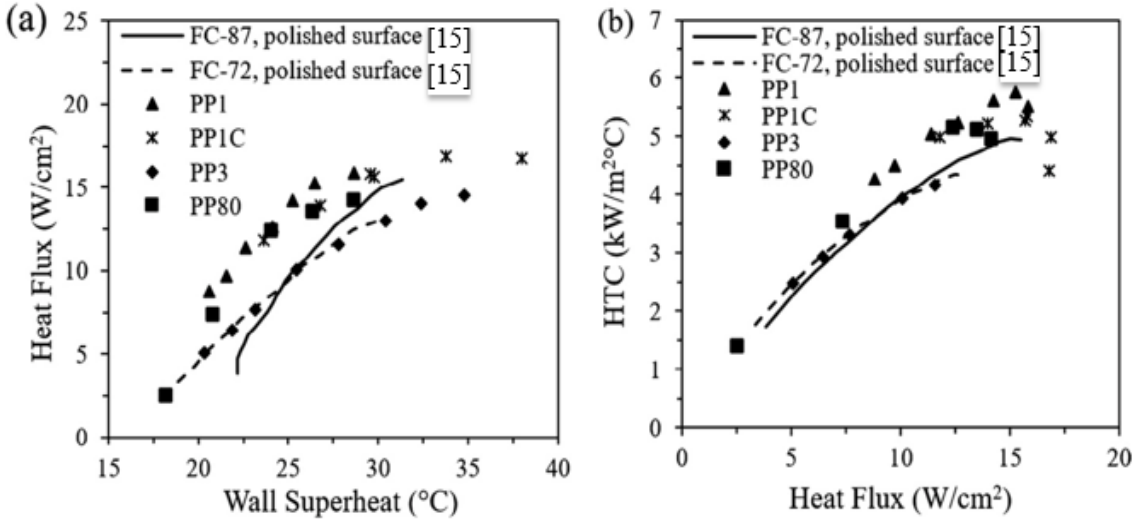

Figure 8. a) Pool boiling curve and b) HTC for tested refrigerants [13].

An extensive study on the effect of channel width and channel depth in microchannel surface while keeping the fin length constant was conducted by Jaikumar and Kandlikar [14]. They used an open microchannel copper surface with porous fin tops for additional nucleation sites and tested FC-87 as the working fluid. The authors identified a channel width-to-depth ratio as an important parameter for performance improvement as shown in Table 1. As shown in Figure 11, test chip 3 with a channel width-to-depth ratio of 1 had the best performance with CHF of 37 W/cm^2, which is 270% enhancement in CHF compared to a plain chip.

Table 1. Comparison of CHF enhancement for FC-87 and water [14].

Channel width/ Channel depth	$CHF_{enhanced}/CHF_{plain}$	
	FC-87	Water
0.75	2.81	2.2
1	3.36	2.56
1.9	0.9	2.2
1.72	2	2.1
2	2	1.89

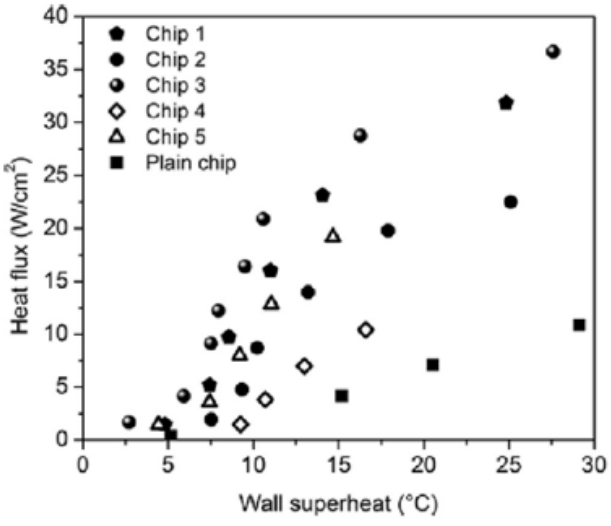

Figure 9. Pool boiling curve for tested chips with FC-87 at atmospheric pressure [14].

The objective of Rainey and You [15] was to study pool boiling performance using saturated FC-72 with a horizontal copper surface (10 mm x 10 mm x 2 mm) incorporating a double enhancement technique that utilizes a 5 x 5 array of square fins varying in length from 0 to 8 mm with a microporous coating as shown in Figure 12. The authors conclude that fins produce resistance to vapor bubble departure which in turn increases the resistance of working fluid for re-wetting in both plain and microporous finned surfaces. The surface temperature of the tip potion of fin was observed to be too low to sustain boiling for plain fin lengths above 5mm.

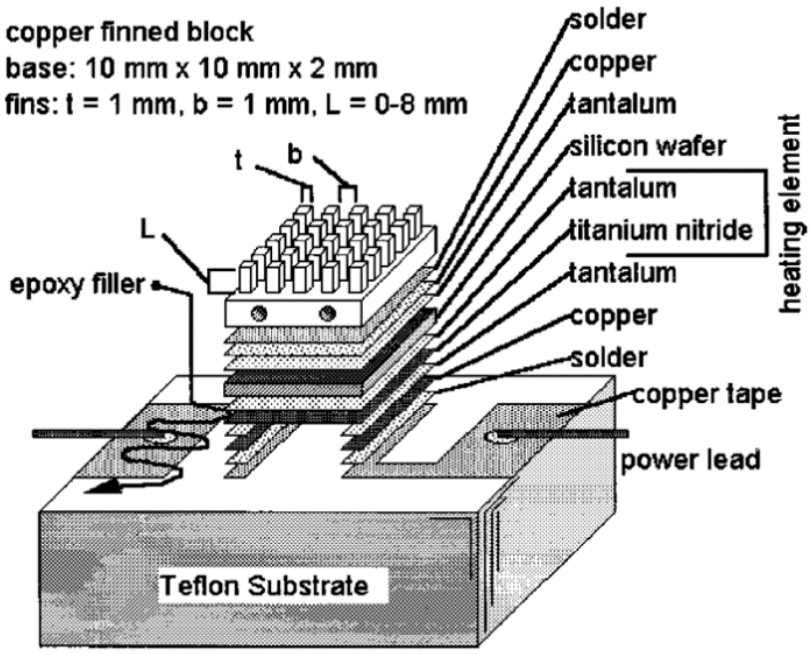

Figure 10. Test heater [15].

2.3 Separate Liquid Vapor Pathways for Boiling Enhancement

Jaikumar and Kandlikar [16] used selective sintering of a microchannel surface to study the performance of separate of liquid vapor pathways. They proposed two enhancement techniques, a) sintered fin tops, and b) sintered channels as shown in Figure 13.

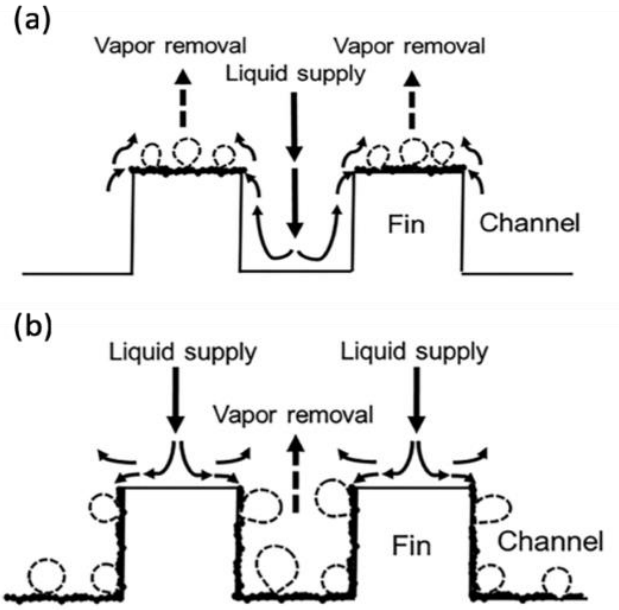

Figure 11. a) Sintered fin tops and b) Sintered channels [16].

In Type (a), nucleation occurs on fin tops whereas liquid addition is through the channel region. In Type (b), a bubble nucleates inside the channel and liquid addition takes place through the fin tops. The wall superheat at the fin top is always lower than that of a channel surface, preventing bubble nucleation at high heat flux on the fin tops and sustaining separate liquid vapor pathways. Sintered channels 300 μm wide yielded a CHF of 420 W/cm^2 at a wall superheat of 1.7°C, which is 228% enhancement of CHF compared to plain chip.

Mahamudur et al. [17] performed experiments on a bi-conductive surface comprising of low conductivity epoxy, periodically arranged and embedded into a high conductivity copper substrate as shown in Figure 14 (a). The test chips varied by the number of epoxy divisions per centimeter in copper substrate. These bi-conductive surfaces promote HTC and CHF. Bubbles

nucleate near the center of a copper substrate, while epoxy remains wetted during boiling and suppresses nucleation. Thus, improving CHF from 116 W/cm^2 for plain copper surface to 230 W/cm^2 for bi-conductive surfaces by creating a separate flow for liquid rewetting and vapor escape as seen in Figure 14(e).

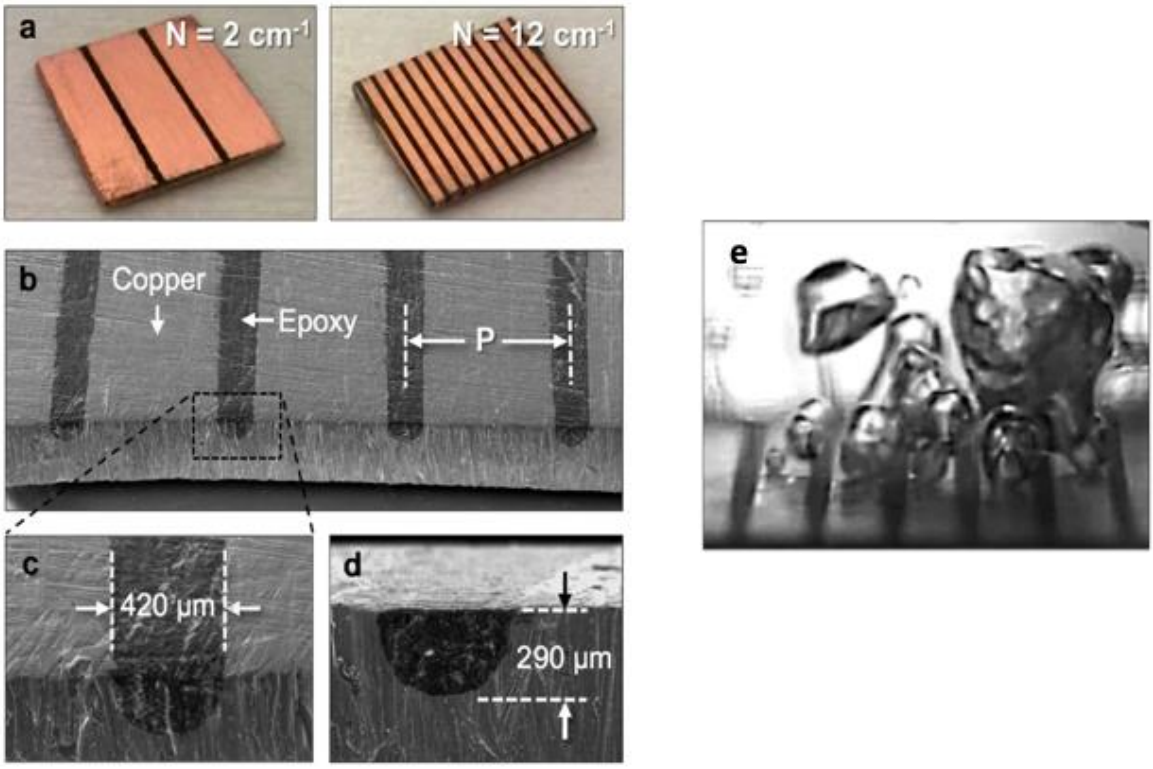

Figure 12. a)Bi-conductive fabricated surfaces, (b-d) SEM image of epoxy divisions in copper substrate, e) high speed image of bi-conductive surface [17].

Jaikumar and Kandlikar [18] proposed an enhancement structure with feeder channels (FC) on the heater surface that supply liquid from bulk towards the nucleation region (NR), as shown in Figure 15(a). Figure 15(b) shows the feeder channels directly impinging towards the nucleation sites and the bubbles departing from nucleating region only. The spacing between the nucleation regions is governed by the bubble departure diameter, so as to avoid lateral bubble coalescence and continuous formation of separate liquid vapor pathway. It was observed that chip (NRFC-3) with a CHF of 394 W/cm^2 and a wall superheat of 5.5°C was obtained with spacing in between the nucleation region was equal to the bubble departure diameter.

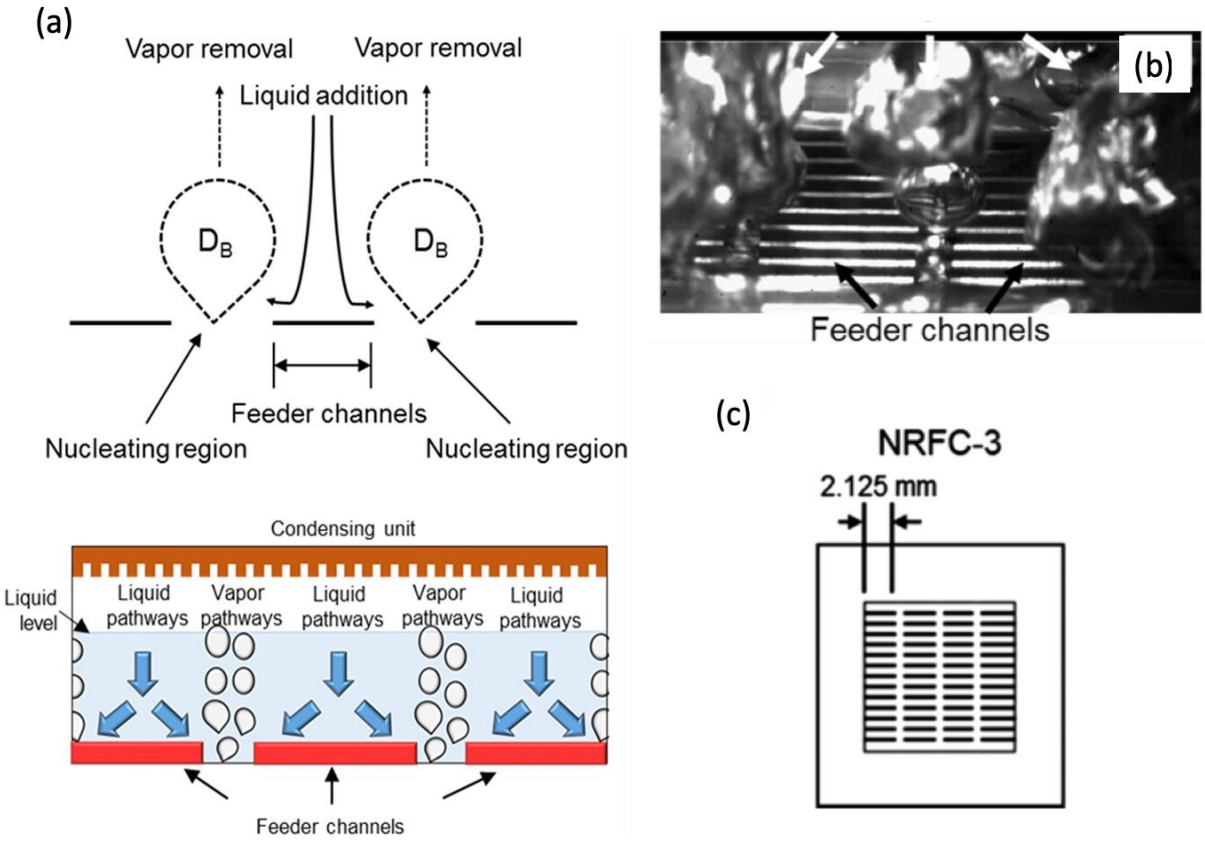

Figure 13. a) Schematic of separate liquid vapor pathway on NRFC configuration, b) picture of bubbles nucleating from nucleation region and the feeder channels, c) Top view of NRFC-3 chip [18].

Hayes et al. [19] performed pool boiling experiments on aluminum heater surfaces with hollow conical structures (HCS) using additive manufacturing for regulating vapor removal. It was observed that the top hole in the HCS governed the direction of liquid and vapor flow. If the top hole diameter is greater than the bubble departure diameter, vapor escapes naturally from the top and liquid enters from the side holes. If the top hole is smaller than the bubble departure diameter, liquid enters from top and vapor escapes from the side holes as shown in Figure 16. The authors obtained an HTC of 190 kW/m²-°C with miniaturized HCS with microchannels, representing a 4-fold increase in HTC compared to a plain aluminum surface.

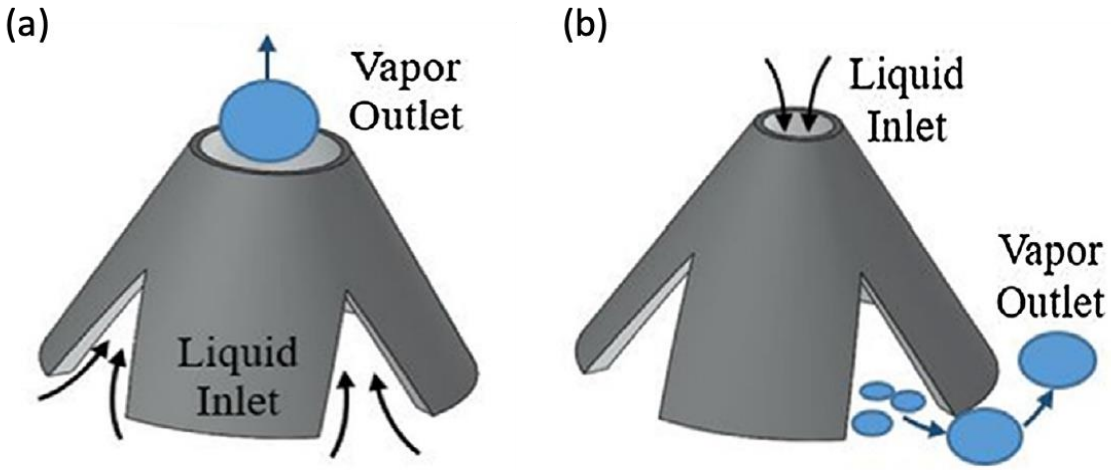

Figure 14 Pathway a) liquid entering from side holes and vapor exits from top hole, b) liquid entering from top and vapor exits from the side holes [19]

2.4 Pool Boiling of Scaled Heater

Kwark et al. [20] studied the effect of heater orientation and heater size on the pool boiling performance. The authors experimented with different heater sizes (0.75 cm x 0.75 cm, 1.0 cm x 1.0 cm, 1.5 cm x 1.5 cm, and 2.0 cm x 2.0 cm) and two different configurations (uncoated and Al_2O_3 nanoparticle coated) at atmospheric pressure with water as the working fluid. A decrease in CHF is observed with increase in heater size. The author believes this is due to larger heaters offering a longer resistance path for the fluid to the hot spots which leads to lower CHF. As shown in Figure 17 it is observed that CHF decreases with increasing heater area.

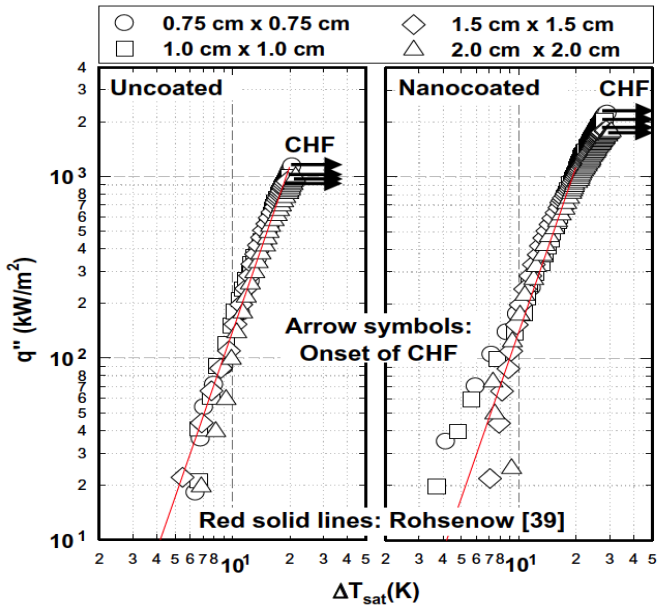

Figure 15. Effect of heater size on pool boiling curve of pure water [20].

Rainey and You [21] experimentally studied the effect of heater size by testing differently sized copper surfaces of 1 cm x 1 cm, 2 cm x 2 cm, and 5 cm x 5 cm with saturated FC-72. Experiments were conducted on plain and microporous coated copper surfaces. The q''_{CHF} values for 1-cm^2, 4-cm^2 and 25-cm^2 were observed to range from 13.2–16.0 W/cm^2, 12.6–13.1 W/cm^2, 12.9–13.2 W/cm^2, respectively. As shown in Figure 18 1-cm^2 plain and microporous surface both have slightly higher q''_{CHF} than 4-cm^2 and 25-cm^2 surfaces.

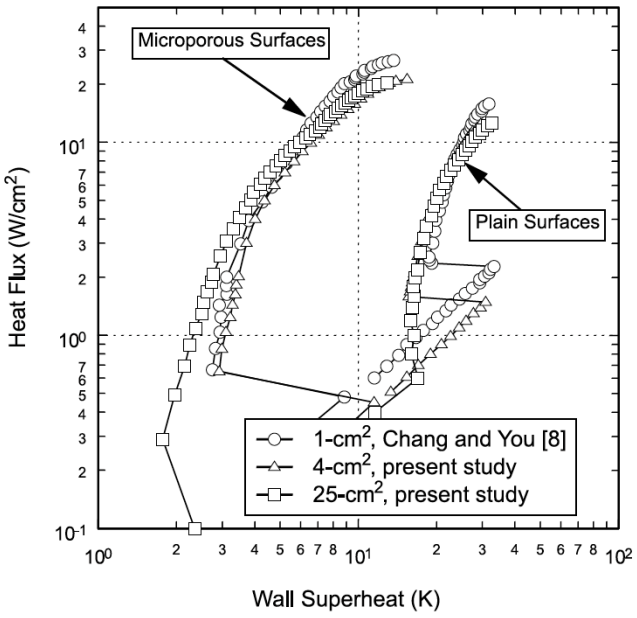

Figure 16. Pool boiling curve for 1-cm², 4-cm² and 25-cm² heater surface [22].

2.5 Scope of Work

This research focuses on enhancing the pool boiling performance of a plain copper chip with a boiling surface of 34.5 mm x 32 mm using PP1, PP1C and FC-87 dielectrics at atmospheric pressure. A very few previous work have studied scaled heater sizes using dielectrics as the working fluid.

As noted from the literature review, microchannel surfaces have a huge impact of enhancing the CHF with low wall superheat temperatures. A similar microchannel surface is implemented in the current study to understand the increase in pool boiling performance of microchannel surface over plain copper surface for a larger heater size.

Separate liquid vapor pathways have a significant effect on enhancing the CHF due to continuous supply of liquid to the heater surface. The novelty of the work stems from using additive manufacturing technique for creating external enhancement structures for facilitating structured vapor removal and liquid supply to heater surface.

3. Experimental Setup

3.1 Test Section

The dimensions of the test section used in this study are 34.5 mm x 32 mm boiling surface in the middle of a circular copper chip of 68 mm diameter as shown in Figure 19. The test chip used in this study consists of a plain copper chip and a microchannel chip. The parameters of microchannels used in this study are channel width, channel depth, and fin width of 500 µm, 400 µm and 200 µm, respectively.

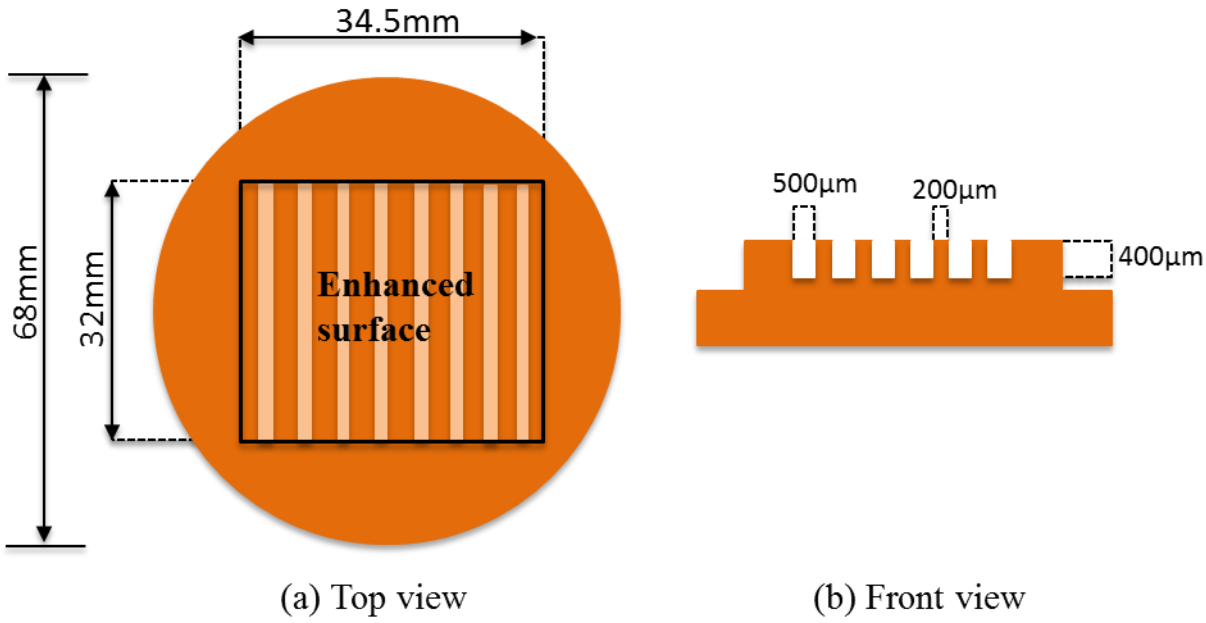

Figure 17. Test section a) Top view, b) Front view.

Joule heating using four cartridge heaters of 120 W each heats the copper heater block of 34.5 mm x 32 mm and a 40 mm projection. Three 0.8 mm holes are drilled in the copper heater block which are 15 mm deep and 5 mm apart to accommodate calibrated K-type thermocouples, T_1, T_2 and T_3 as shown in Figure 20. Another 0.7 mm hole is drilled in the center (2 mm below the heater surface) of the test section to accommodate thermocouple T_c for measuring the surface temperature from the known heat flux.

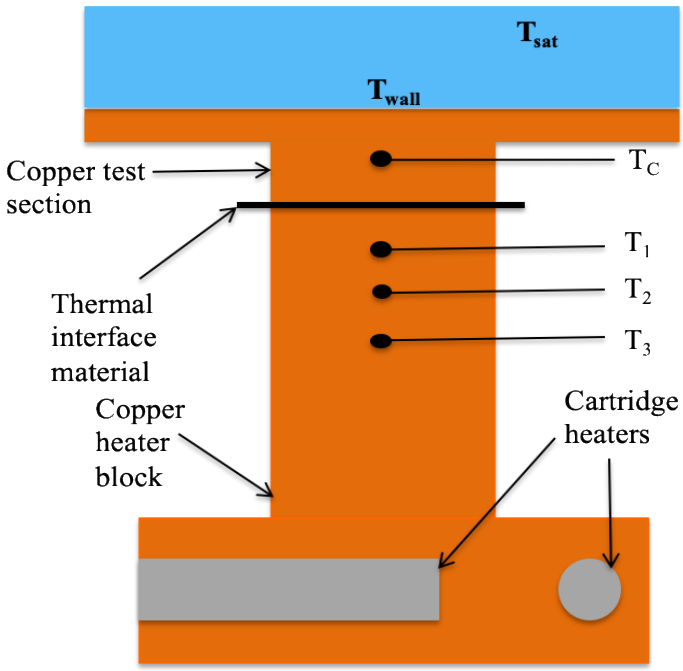

Figure 18. Schematic of heater section.

The heater assembly as depicted in Figure 21 consists of the copper test chip, gasket and garolite block held together using 4-40 x 3/8" socket cap screws arranged in a circular pattern.

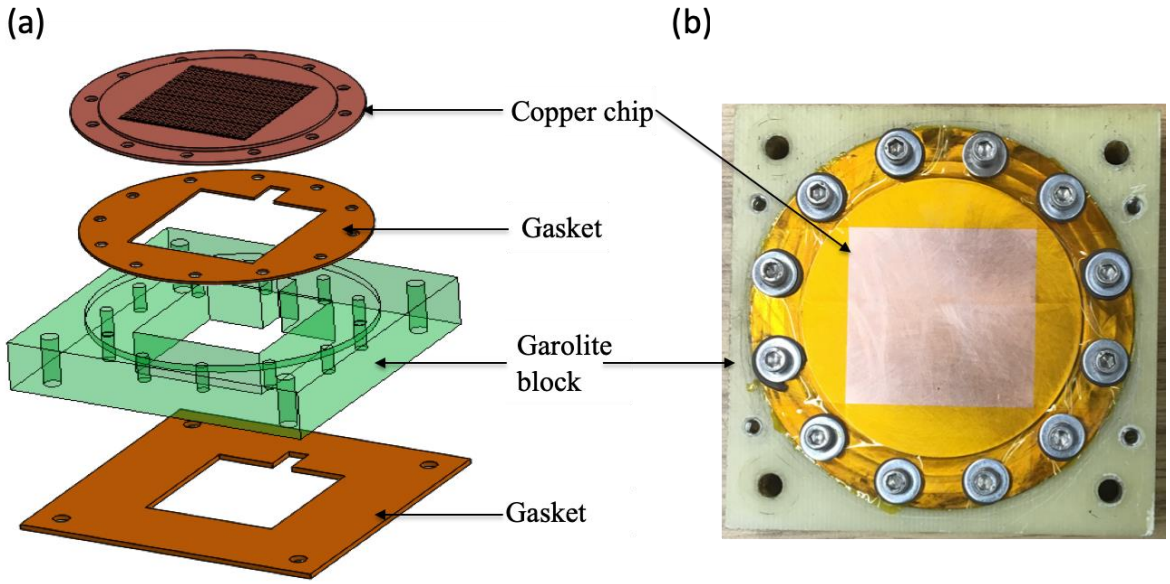

Figure 19. a) Schematic heater assembly, b) Actual Image of heater assembly.

3.2 Volcano Manifold

A volcano manifold is bolted to the garolite block of the heater assembly. The volcano manifold consists of 3 x 3 array of hollow conical structures (HCS) each having base length of 9.75 mm, top hole diameter of 3 mm and height 5.75 mm. The HCS is raised to a height of 2 mm and have 1 mm gap below for regulating the flow of liquid to the heater surface as shown in Figure 22. 1 mm holes are drilled between each volcano structure for rewetting the heating surface. The array of HCS covers the entire boiling surface of 34.5 mm x 32 mm. The array of hollow conical structures together is called the volcano manifold.

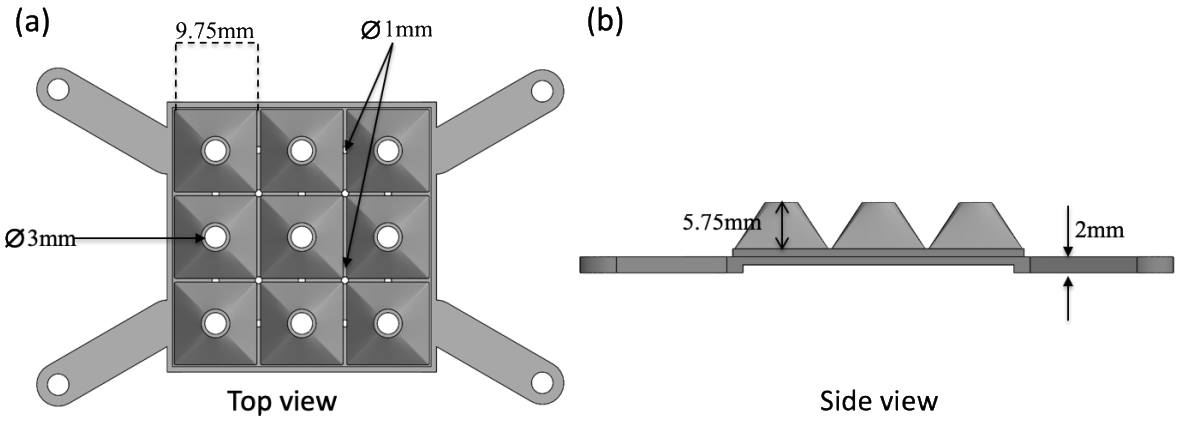

Figure 20. Volcano manifold, a) Top view, b) Side view.

The volcano manifold is manufactured using the fusion deposition additive manufacturing technique. Original Prusa I3 Mk3S 3D printer was used to manufacture the volcano manifold using Proto-pasta's High Temperature PLA (HTPLA) v2.0. The HTPLA is originally translucent in color. After the 3D structure is printed, HTPLA undergoes heat treatment at 90^{o}C for 45 minutes and turns opaque. HTPLA has a heat deflection temperature for 120^{o}C or more, unlike PLA which has low heat deflection temperature of 55^{o}C [23].

Figure 23 shows the volcano manifold with the heater assembly. The flow of liquid and vapor above the heater surface is regulated by placing the volcano manifold on top of the heater surface. The hollow conical structures have holes on the top that are included for removal of

vapor bubbles generated under the volcano manifold. A 1-mm gap is provided below the hollow conical structures for the bulk liquid to rewet the heater surface.

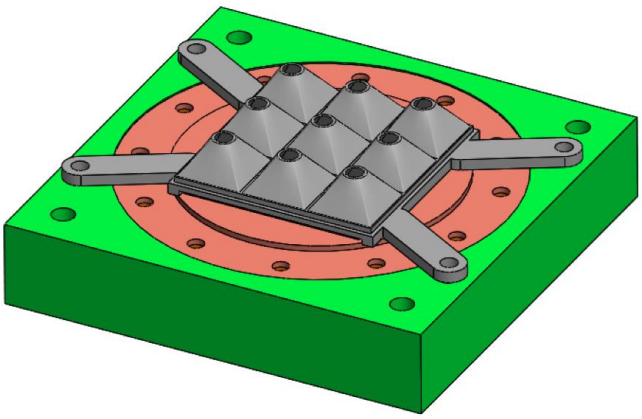

Figure 21. Heater assembly with volcano manifold.

3.3 Dual Taper Manifold

A dual taper manifold is similarly bolted to the garolite block of the heater assembly like the volcano manifold. As shown in Figure 24 the top surface of the dual taper manifold has 3 slots. Two slots serve the purpose of liquid inlet, whereas the middle slot serves the purpose of vapor removal. The liquid inlet slots and vapor removal slots are 1 mm x 34.5 mm and 1.5 mm x 34.5 mm, respectively. A taper of 15^{o} at inlet is provided to reduce the resistance to the flow of liquid for reaching the heating surface. At the bottom surface, a similar 15^{o} taper is provided for vapor removal. The height of the dual taper manifold is 5mm. Also, the dual taper manifold is raised by 0.5 mm for regulating the flow of liquid to the heater surface.

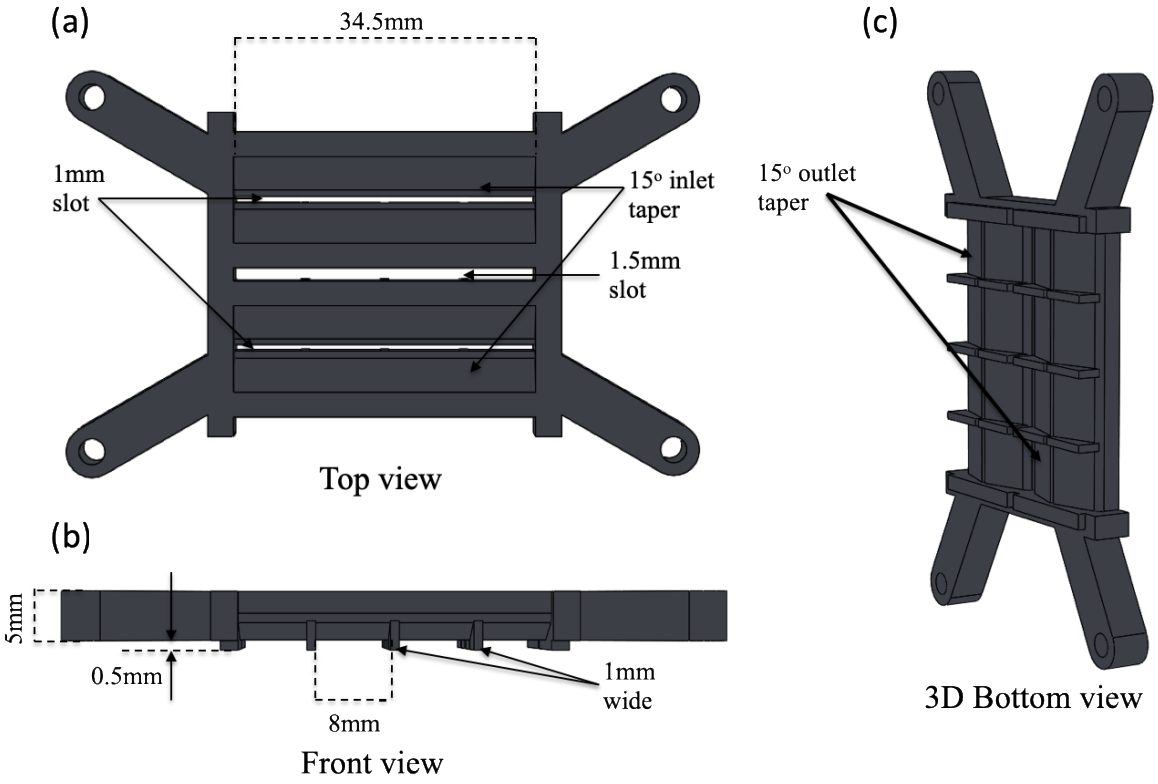

Figure 22. Dual taper manifold, a) Top view, b) Front view, and c) 3D Bottom view.

The dual taper manifold is fabricated using stereolithography additive manufacturing technique. The Forms2 printer was used to manufacture the dual taper manifold for a smoother surface finish to reduce the resistance for liquid and vapor flow. The resin bath used for constructing the 3D structure is Black V4 (FLGPBK04) resin. After the dual taper manifold is constructed, it undergoes a post-curing process. The 3D structure is placed in isopropyl alcohol (IPA) bath for 30minutes and then undergoes curing under 405 nm wavelength light at 60°C for 30 minutes [24]. Figure 25 (b) shows the dual taper manifold bolted to the heater assembly.

(a) (b)

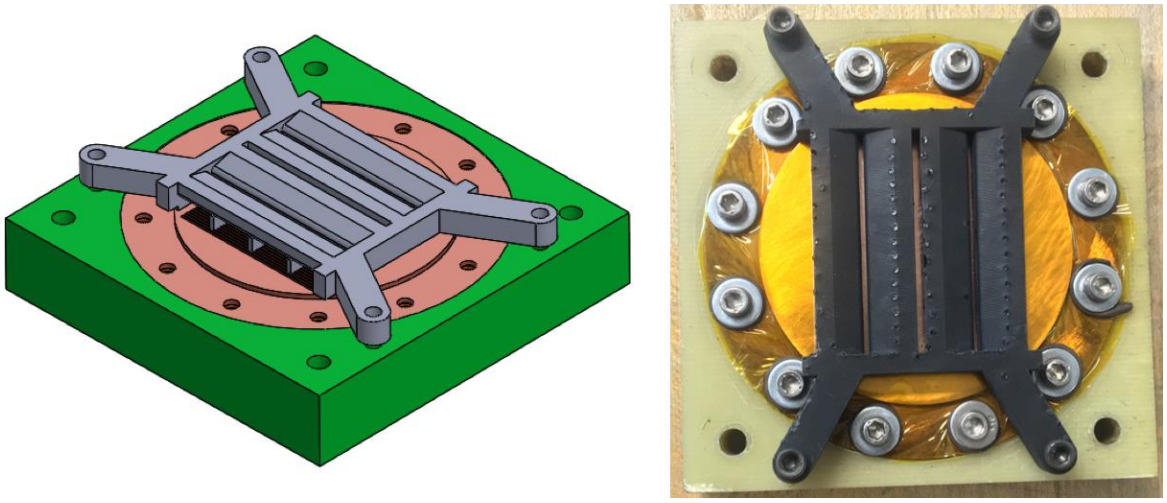

Figure 23. Heater assembly with dual taper manifold, a) Design and b) Actual image.

3.4 Pool Boiling Setup

A rectangular aluminum block of 6 inch x 6 inch x 3 inch seen in Figure 26 is used for the pool boiling setup. Copper coil (condenser) containing 9 turns with each turn's internal diameter being 26.4 mm acts as a heat exchanger with an inner and outer diameter of 4.8 mm and 6.3 mm, respectively. The condenser is connected to an external chiller that supplies water temperature -30°C to 150°C for the entire duration for all experiments. The top surface of the aluminium block is mounted with a pressure gauge, two valves and a K-type thermocouple. The K-type thermocouple extends to the bottom of the aluminium block to measure the working fluid's temperature. One valve is used for connecting the aluminium block to the vacuum port & the other valve acts as an inlet to feed the working fluid inside the setup.

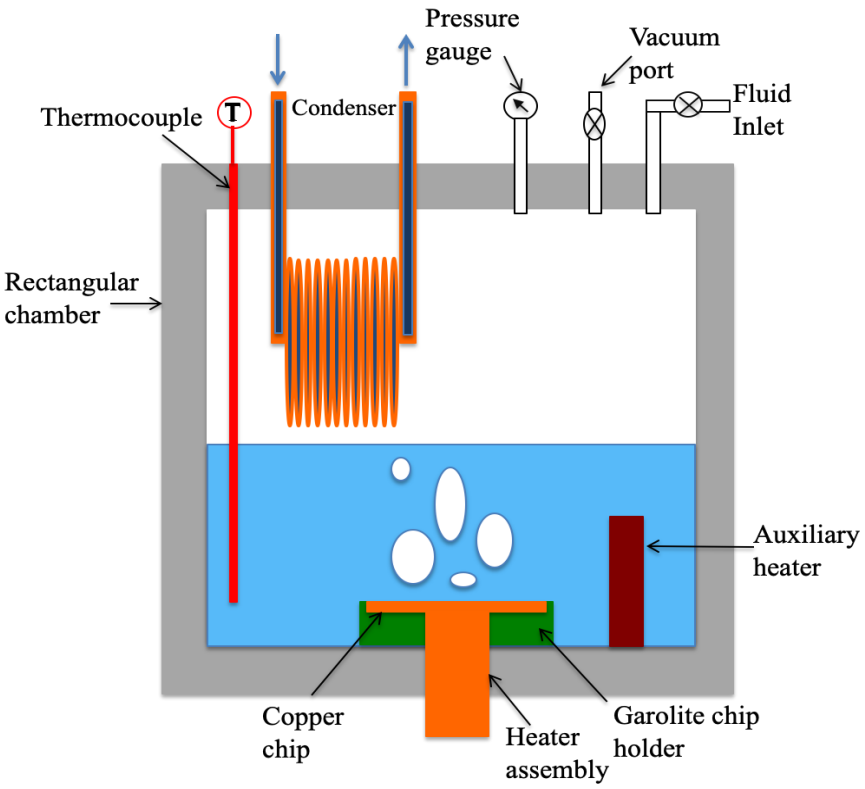

Figure 24. Schematic pool boiling setup.

Aluminium plates (8x8) inches and 9.5 mm thick borosilicate glass are used to hold the central block in its place as shown in Figure 27.

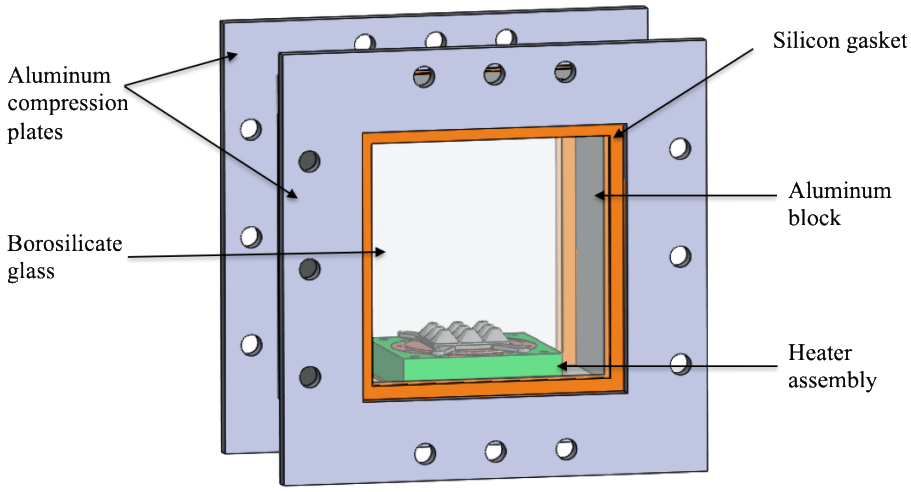

Figure 25. Pool boiling setup.

These high temperature borosilicate glasses are used for better visualization. Silicone gaskets are used in addition to the borosilicate glass to ensure a leak free setup. The bottom surface of the aluminium block has of two grooves; one of which is used for an auxiliary heater (120VDC,

200W) and the other one for the copper heater block to contact the test chip. The aluminium compression pates and silicon gasket held the test setup together, but also ensured its horizontal orientation during the experiment. Contact resistance is minimized by using an arctic silver Thermal Interface Material (TIM) between the copper block and the test chip.

3.5 Experimental Procedure & Setup Validation

- It is crucial to have in place a completely sealed pool boiling setup while using refrigerants as the working fluid. In order to ensure the test setup is sealed, the working fluid was poured into it and allowed to stand for a 24-hour period. The setup was then checked for leaks, the chamber was evacuated and refilled with the working fluid via the inlet valve.
- Every test is preceded by a roughness measurement of the boiling surface using a confocal laser scanning microscope at 10X magnification.
- The test chip is bolted to the fabricated garolite chip holder using a 4-40x3/8" socket cap screw. Garolite is used due to its low thermal conductivity and ability to withstand high temperatures up to 165°C.
- 8-32x1-3/4" socket head bolts are used for mounting the heater assembly to the bottom flange of the aluminum block.
- The test setup was filled with refrigerant via the inlet valve.
- The working fluids used in the study are PP1, PP1C, FC-87. 420 mL of refrigerant is consistently used for each experiment.
- The chamber pressure was then reduced to 101.3 kPa.
- The copper block and auxiliary heaters are then turned on while simultaneously initiating a LabVIEW program.

- The LabVIEW program uses a National Instruments cDAQ-9172 and a MOD-9211 is used to record temperatures.
- An initial voltage from the DC power supply is increased with 4V steps which subsequently is reduced to 2V at higher heat fluxes.
- The temperature of the water circulating within the condenser along with the power to the auxiliary heater is continuously adjusted at each subsequent step until atmospheric pressure is attained.
- At each step, data is recorded as soon as the experiment reaches steady state. The data recording process takes place for 20 seconds at a 4Hz sample rate.
- The experiments are conducted until critical heat flux (CHF) is achieved.

4. Data Acquisition

Data reduction here was similar to that found in previously published works [10–14,25,26].

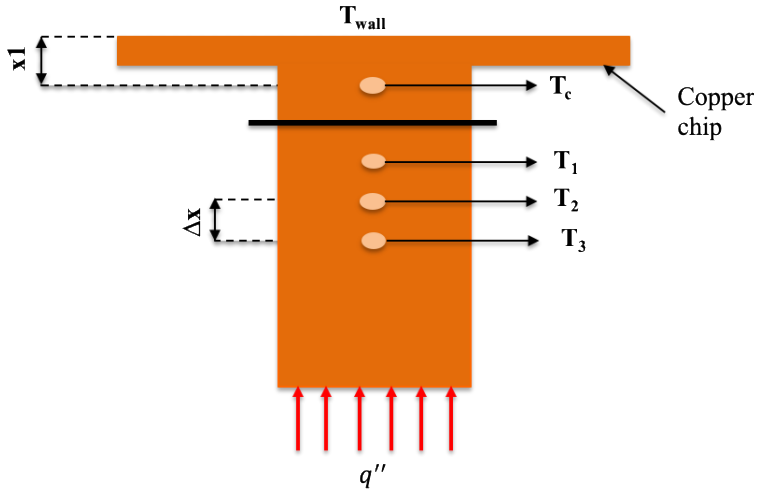

Figure 26. 1-D Conduction in copper block.

Heat flux through the copper block is calculated by assuming Fourier's law of 1-D conduction.

$$q''_{block} = -k_{Cu}\frac{dT}{dx} \tag{1}$$

Where, q''_{block} is the heat flux, k_{Cu} is the thermal conductivity of copper, dT/dx is the temperature gradient. The temperature gradient dT/dx was estimated using Taylor's backward series approximation and expressed as:

$$\frac{dT}{dx} = \frac{3T_1 - 4T_2 + T_3}{2\Delta x} \tag{2}$$

Where, T_1, T_2 and T_3 are the temperatures corresponding to the three thermocouples in the copper block as shown in Figure 28 and Δx is the spacing between the thermocouples, 5 mm. A heat loss study previously performed in which the chip surface was insulated is included in the data reduction [27]. Wall superheat values are used for calculating heat loss at each data point. The effective heat flux ($q"_{effective}$) is given by deducting heat loss ($q"_{loss}$) from the calculated heat flux.

$$q''_{effective} = q''_{block} - q''_{loss} \tag{3}$$

The surface temperature (T_{Wall}) can be calculated using effective heat flux ($q"_{effective}$) and Eq. (1) as

$$T_{wall} = T_c - q'' \left(\frac{x1}{k_{Cu}}\right) \tag{4}$$

Where, T_{wall} is the surface temperature of the boiling surface, x1 is the distance between the boiling surface and thermocouple T_C, measuring 4 mm. The heat transfer coefficient (HTC) is calculated from effective heat flux at the surface of the copper chip and wall superheat, ΔT_{sat}.

$$h = \frac{q''}{\Delta T_{sat}} = \frac{q''_{effective}}{T_{wall} - T_{sat}} \tag{5}$$

5. Uncertainty Analysis

An uncertainty analysis was performed similar to that of [10, 29, 30]. Thermocouple calibration, thermal conductivity of copper and length measurements between thermocouples contributed to the uncertainty calculations. There are two types of errors that rise during experimentation: 1) bias error, 2) precision error. The cumulative total of bias and precision error can be expressed as:

$$U_y = \sqrt{B_y^2 + P_y^2} \tag{6}$$

Where U_y is the total uncertainty, B_y is the bias error and P_y is the precision error. The thermocouples precision error is calculated by first calculating standard deviation of the temperature readings recorded during calibration of thermocouples over a range of steady state temperature conditions. The average of the standard deviation taken at each steady state temperature was then doubled to obtain a 95% confidence interval. Whereas, bias error of thermocouples is calculated by the standard deviation of measured values from the mean during testing.

The error propagation is determined through temperature gradient, heat flux, surface temperature, wall superheat and HTC by using the following equation:

$$U_p = \sqrt{\sum_1^n \left(\frac{\partial p}{\partial a_i} u_{ai}\right)^2} \tag{7}$$

Where $U_p$is the uncertainty in parameter p, and u_{ai} is the uncertainty of parameter a_i. Eq. (8) expresses the percent uncertainty in heat flux.

$$\frac{U_{q''}}{q''} = \sqrt{\frac{(U_k)^2}{k^2} + \frac{(U_{\Delta x})^2}{\Delta x^2} + \frac{9(U_{T_1})^2 + 16(U_{T_2})^2 + (U_{T_3})^2}{(3T_1 + 4T_2 + T_3)^2}} \tag{8}$$

The uncertainty in heat flux (q'') for plain copper chip tested for refrigerants PP1, PP1C and FC-87 are plotted in Figure 29. The uncertainty in heat flux was estimated as 6.5%, 6.0% and 5.7% for PP1, PP1C and FC-87, respectively for a plain copper chip at CHF.

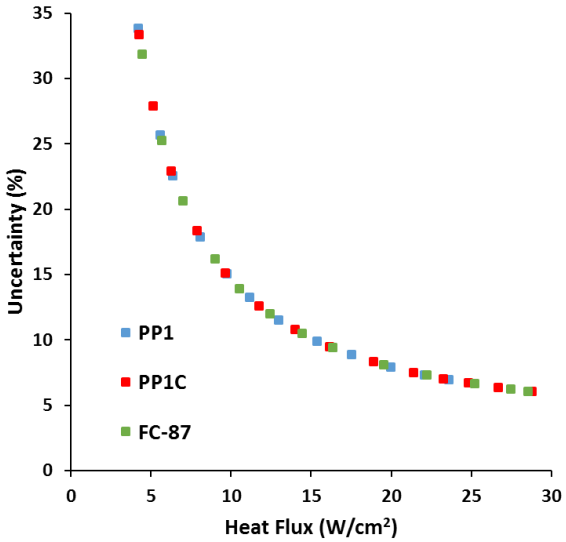

Figure 27. Variation in uncertainty with increasing heat flux for tested refrigerants with plain chip.

Fourier's law of 1-D conduction is used in determining heat flux through the copper heater block. The temperature profile over the length of the copper heater block as shown in Figure 30. Figure 30 shows the temperature distribution for heat flux values of 6.2 W/cm^2, 11.7 W/cm^2, 18.8 W/cm^2, and 26.5 W/cm^2 varying from T_3 to T_1 for a plain copper chip surface. The plot depicts a linear temperature profile and calculated R^2 values, all of which are very close to 1. Thus the linear temperature profile confirms the assumption that heat flux through the heater block is transferred through 1D-conduction with negligible losses.

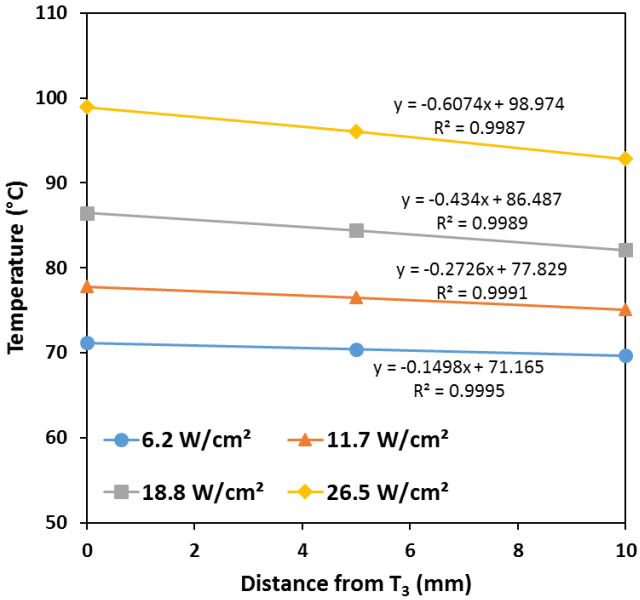

Figure 28. Temperature variation over heater block for various heat fluxes.

6. Results & Discussions

The primary objective of this study is to provide the baseline understanding of heater scalability and provide an effective means for regulating the flow of liquid over the boiling surface without changing the characteristics of the test section. Each of the three refrigerants (PP1, PP1C & FC-87) are tested with a plain copper chip and a microchannel chip at atmospheric conditions. Further, these refrigerants are tested with volcano and dual taper manifolds with a plain chip and a microchannel chip.

Tests have been performed under increasing heat flux by supplying an external power and increasing it at regular interval. The data is recorded when the steady state in temperature is attained at each heat flux. Each test is performed until CHF is reached; it is then stopped to avoid the overheating of the heater surface.

6.1 Plain Copper Chip

A plain copper chip with a 34.5 mm x 32 mm boiling surface was tested with PP1, PP1C, and FC-87 as the working fluids at atmospheric pressure. Figure 31 shows the boiling curve for tested refrigerants with plain chip. A CHF of 23.6 W/cm^2 and 28.7 W/cm^2 at a wall superheat of 30.8°C and 35.9°C was achieved for PP1 and PP1C respectively. However, with FC-87 comparatively a higher CHF of 30.5 W/cm² at wall superheat of 30.2°C was achieved. The heat transfer coefficient for PP1, PP1C and FC-87 for the plain chip was found as 7.6 kW/m² °C, 8.0 kW/m² °C, and 10.0 kW/m² °C, respectively.

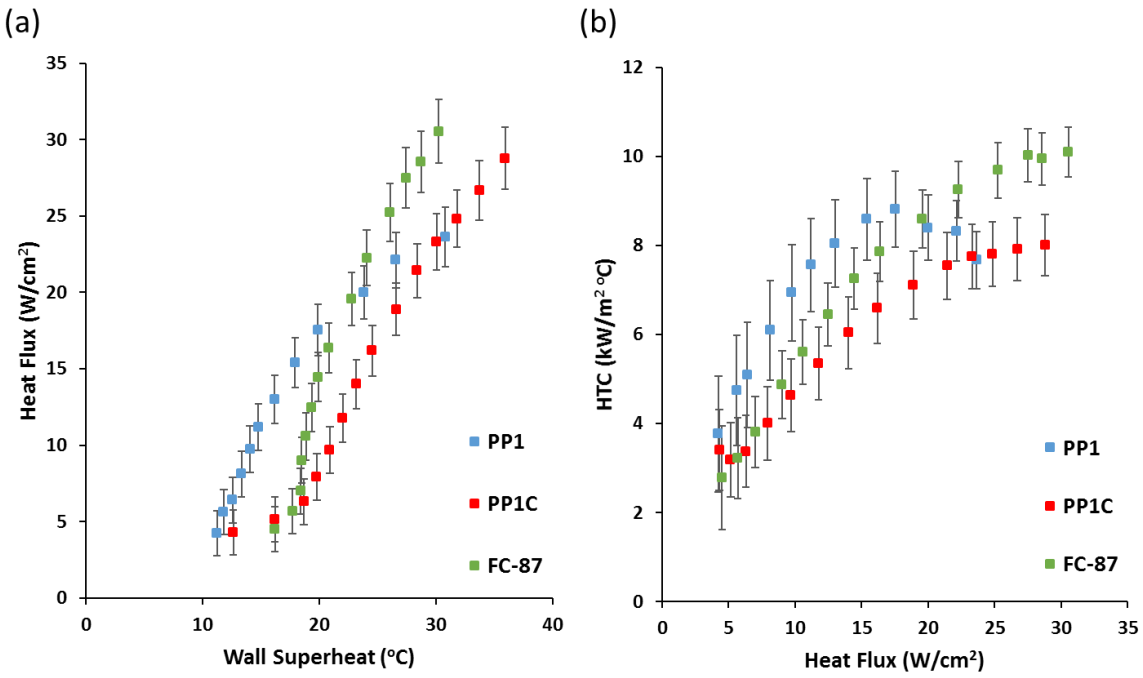

Figure 29. (a) Pool boiling curve and (b) HTC for tested refrigerants with plain copper chip.

Similar trends of decrease in HTC just before reaching CHF is observed in literature [13]. At a higher heat flux bubbles depart from the surface more frequently and this increases bubble coalescence, creating more vapor columns. At CHF, these vapor columns create a vapor blanket over the surface. This transition from vapor columns to attaining CHF is likely the reason for a decrease in HTC in a higher heat flux region. This could also be the reason for an increase in surface temperature at higher heat fluxes with a small increase in given input. High-speed images of vapor removal from a plain copper chip surface with PP1 working fluid at different heat fluxes are shown in Figure 32. With increments in heat flux, intense bubble activity was observed on the heater surface. Also, the large vapor lumps were departed from the heater surface which are prominently observed from 19 W/cm² to CHF. The dashed line indicates the vapor blanket over aplain copper chip at CHF.

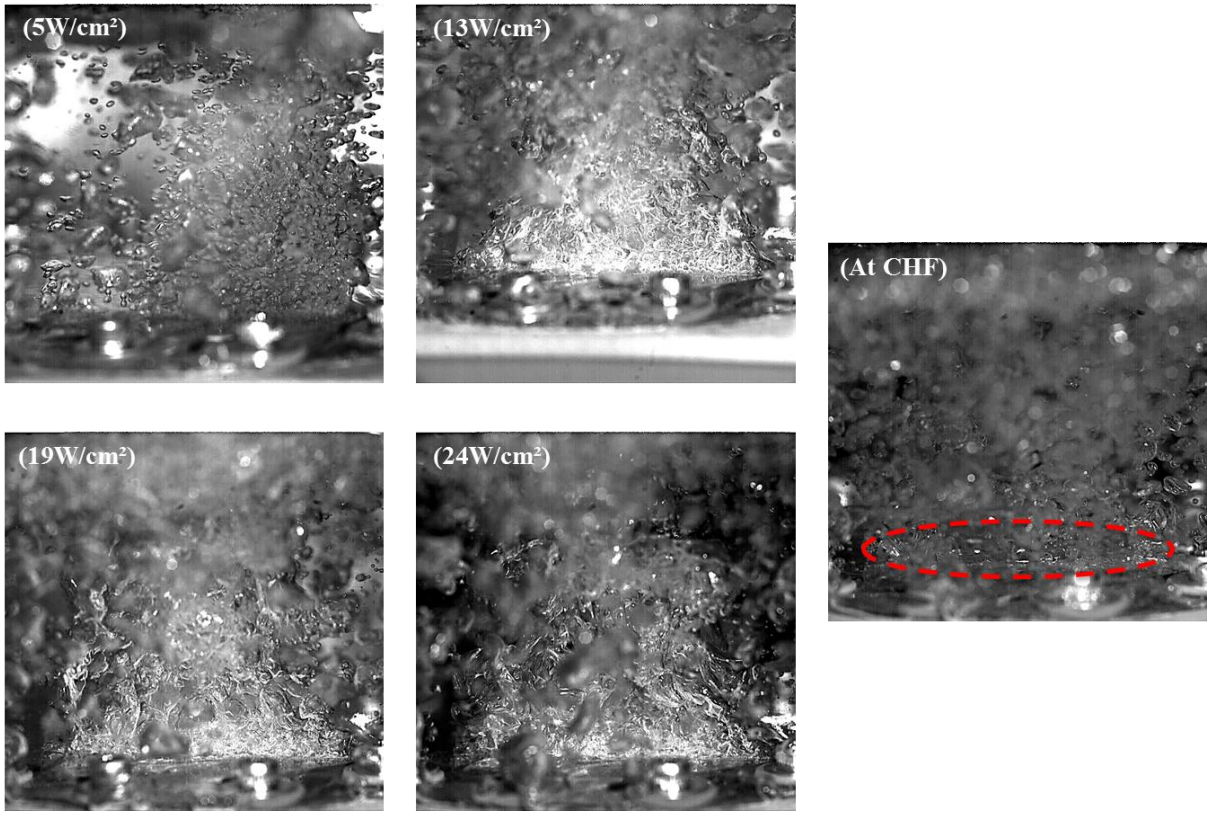

Figure 30. High-speed images of bubbles nucleation over plain copper chip with PP1 at atmospheric pressure at 5 W/cm², 13 W/cm², 19 W/cm², 24 W/cm² and CHF.

6.2 Microchannel Chip

The microchannel chip with channel width, channel depth and fin width of 500µm, 400µm and 200µm, respectively are used in this study. It was observed that PP1, PP1C and FC-87 obtained heat fluxes of 42 W/cm², 40.6 W/cm² and 36.5 W/cm² at a wall superheat of 19.6°C, 26.4°C and 23.6°C, respectively. CHF was not obtained for microchannel chips with all three refrigerants due to the limitations of the test setup. In Figure 33(a), at low heat fluxes a trend of decreasing wall superheat is observed with all three refrigerants and after certain increments in heat flux, the wall superheat starts to increase. It is hypothesized that at low heat fluxes, there is localized boiling over the test section. These localized boiling spots create vapor columns and reduce the wall superheat. With an increase in heat flux, localized boiling increases and boiling starts over the entire surface of the test section which leads to increments in wall superheat with increase in heat flux. The heat transfer coefficient increases with

microchannel chip for all three refrigerants. Table 2 compares the HTC for plain and microchannel chips and shows an enhancement factor calculated at the wall superheat of 19°C. Since the microchannel chips do not attain CHF, this 19°C wall superheat temperature was considered. For a data point not falling on 19°C of superheat, adjacent points were linearly interpolated for HTC estimate.

Table 2. HTC and enhancement factor based of plain chip at 19°C for PP1, PP1C and FC-87.

Refrigerants	Plain chip HTC (kW/m² °C)	Microchannel chip HTC (kW/m² °C)	Enhancement factor
PP1	8.6	19.0	2.2
PP1C	8.4	13.4	1.6
FC-87	8.4	12.7	1.5

The maximum heat transfer coefficients achieved for microchannel chips with PP1, PP1C and FC-87 were 21.8 kW/m² °C, 15.3 kW/m² °C, and 15.4 kW/m² °C, respectively.

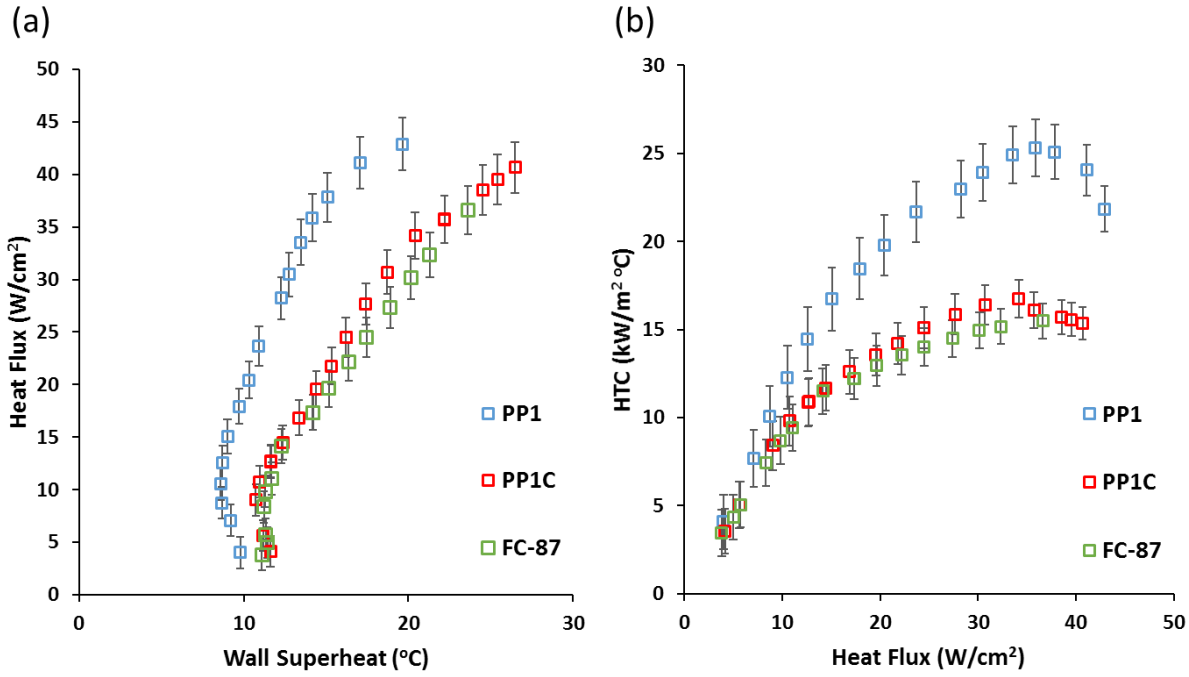

Figure 31. (a) Pool boiling curve and (b) HTC for tested refrigerants with microchannel chip.

Compared to plain chips, microchannel chips showed a large enhancement in both heat flux and heat transfer coefficients (HTC). The microchannels assist in providing an efficient liquid supply to the bubble nucleation sites. This continuous liquid flow in the microchannels help in reducing the wall superheat and thus increasing heat flux and HTC. Similar enhancements were observed in literature [10] for the microchannel chips with smaller boiling surfaces (10 mm x 10 mm).

6.3. Volcano Manifold

The volcano manifold consists of 3 x 3 array of hollow conical structures similar to a volcano having a larger base diameter and a smaller diameter at the top. The array of hollow conical structures together is called the volcano manifold. Figure 34 a) and b) show the volcano manifolds used in this study. The main objective of using the volcano manifold is to direct the vapors through a specific structure to generate the separate liquid vapor pathways without any deposition and/or chemical surface modifications to the test surface. It is hypothesized that this volcano manifold will assist in regulating the flow of refrigerants over the boiling surface by developing independent liquid and vapor flow fields.

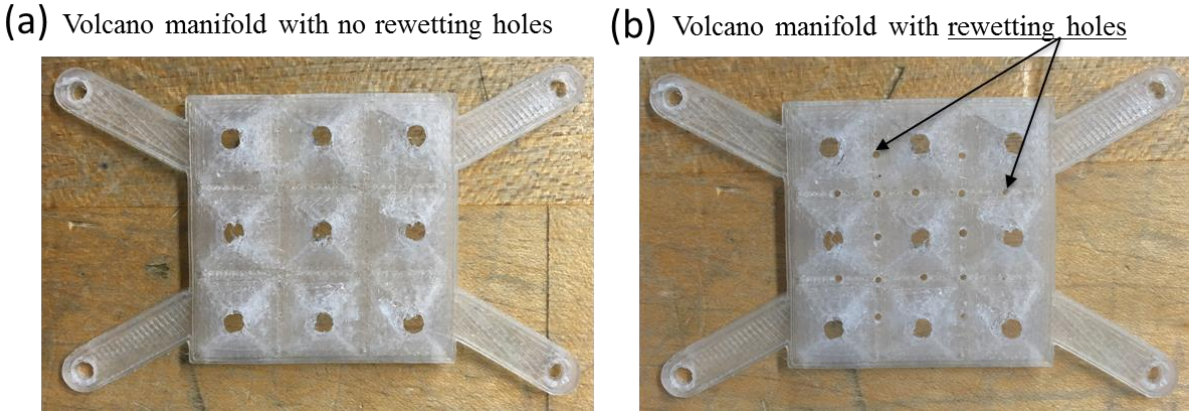

Figure 32. Volcano manifold, (a) No rewetting holes and (b) With rewetting holes.

Initially, the vapor manifold as shown in Figure 34 (a) was bolted on the plain copper chip and was tested to determine whether it assists in increasing the pool boiling performance compared

to a plain copper chip. It was found that as compared to the plain copper chip, the CHF and HTC of the plain copper chip using the volcano manifold (as shown in Fig. 34 a)) was lower when tested with PP1C. It was believed that owing to the larger heater surface dimensions (34.5 mm x 32 mm), the volcano manifold failed to provide the continuous rewetting on the heater surface. This led to a large increment in wall superheat without much enhancement in CHF.

Thus, to increase the liquid supply to the heater surface and to enhance the rewetting, a parametric study was performed in which additional rewetting holes were drilled in the volcano manifold at several locations by maintaining the symmetry along the volcano manifold (as shown in Figure 34 (b)). Three dimensions for rewetting holes were selected based on the bubble departure diameter of the dielectric fluids. The bubble departure diameter for PP1 and PP1C are 1.56mm and 1.37mm respectively [30]. To avoid the escape of vapor through these rewetting holes, the diameters of the holes were less than the departure diameter of a vapor bubble. Thus, to optimize the diameter, three different diameters of 0.635 mm, 1 mm and 1.5 mm of rewetting holes were drilled and the pool boiling tests were performed on a plain copper chip with PP1C as the working fluid. It is evident from Figure 35 that the 1 mm diameter of rewetting hole yielded the highest pool boiling performance giving CHF of 38.3 W/cm² and HTC of 7.8 kW/m² °C. Also, 0.635mm rewetting holes achieved CHF at 30.9 W/cm² due to insufficient supply of liquid to the heater surface. With the help of high-speed images it was observed that vapors escaped through 1.5 mm rewetting holes which was not desirable. Hence, the 1 mm diameter rewetting holes were further used during the testing with other refrigerants and microchannel chips. Additionally, it was observed that, at low heat fluxes, the volcano manifold with holes performs better than the plain chip, but after a certain heat flux, wall superheat increases and the boiling curve for the volcano manifold crosses over the pool boiling curve of the plain chip.

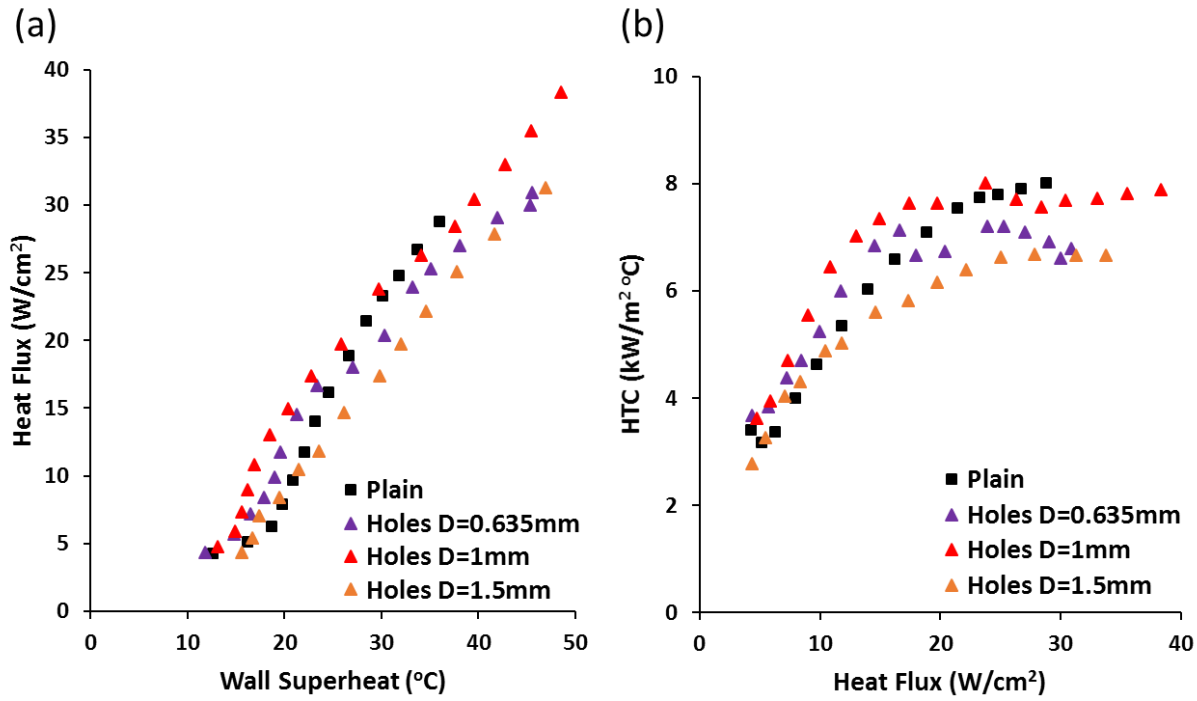

Figure 33. (a) Pool boiling curve and (b) HTC plain chip with PP1C at atmospheric pressure using volcano manifolds with rewetting holes 0.635mm, 1mm and 1.5mm.

6.3.1 Plain Copper Chip with the Volcano Manifold

Plain copper chip was tested with volcano manifold having rewetting holes of 1mm diameter and working fluid as PP1, PP1C and FC-87 at atmospheric pressure. It was observed that PP1, PP1C and FC-87 obtained CHF at 28.1 W/cm², 38.3 W/cm² and 32.5 W/cm², respectively. While heat transfer coefficients on a plain chip of 8.8 kW/m² °C, 7.8 kW/m² °C and 8.7 kW/m² °C for PP1, PP1C and FC-87, respectively as shown in Figure 36.

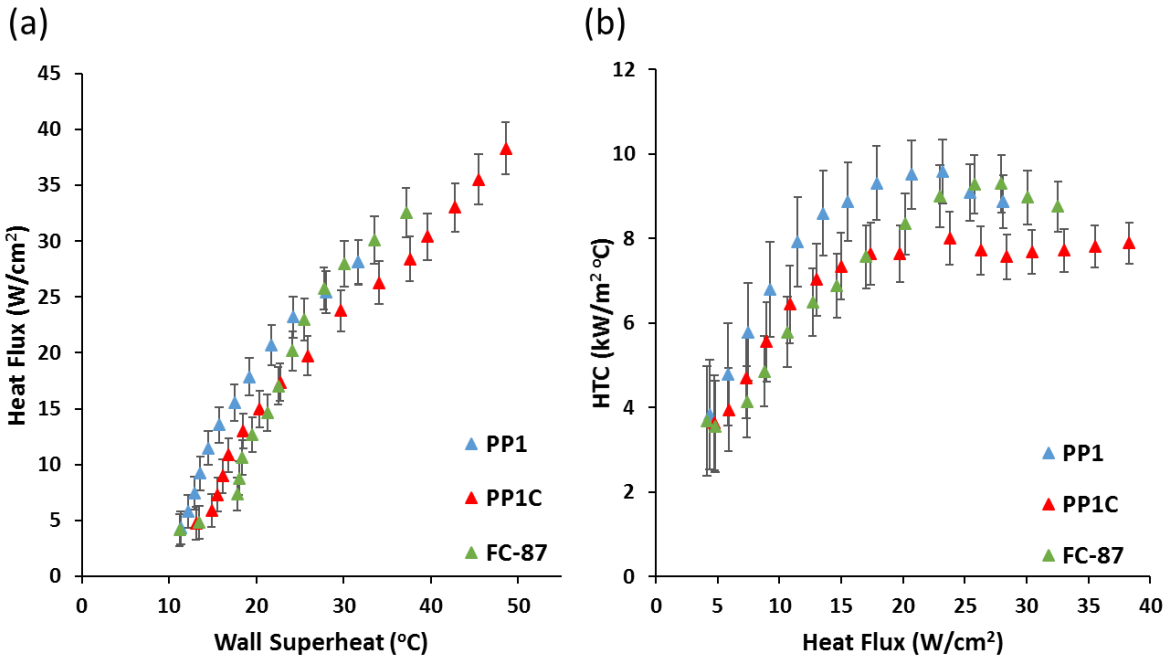

Figure 34. (a) Pool boiling curve and (b) HTC for tested refrigerants with plain chip and volcano manifold with rewetting holes of 1 mm diameter.

Figure 37 shows a schematic representation of how the volcano manifold regulates the flow of liquid over the heater surface creating separate liquid-vapor pathways. The top hole of hollow conical structures enable removal of vapor bubbles generated under the volcano manifold. A gap of 1 mm is provided below the hollow conical structures (HCS) for liquid to flow through the sides and rewet the heater surface.

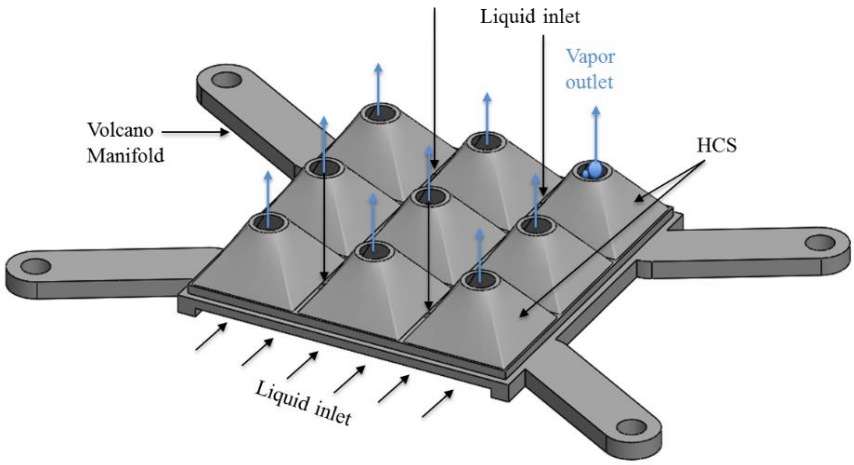

Figure 35. Schematic representation of separate liquid and vapor fields in volcano manifold.

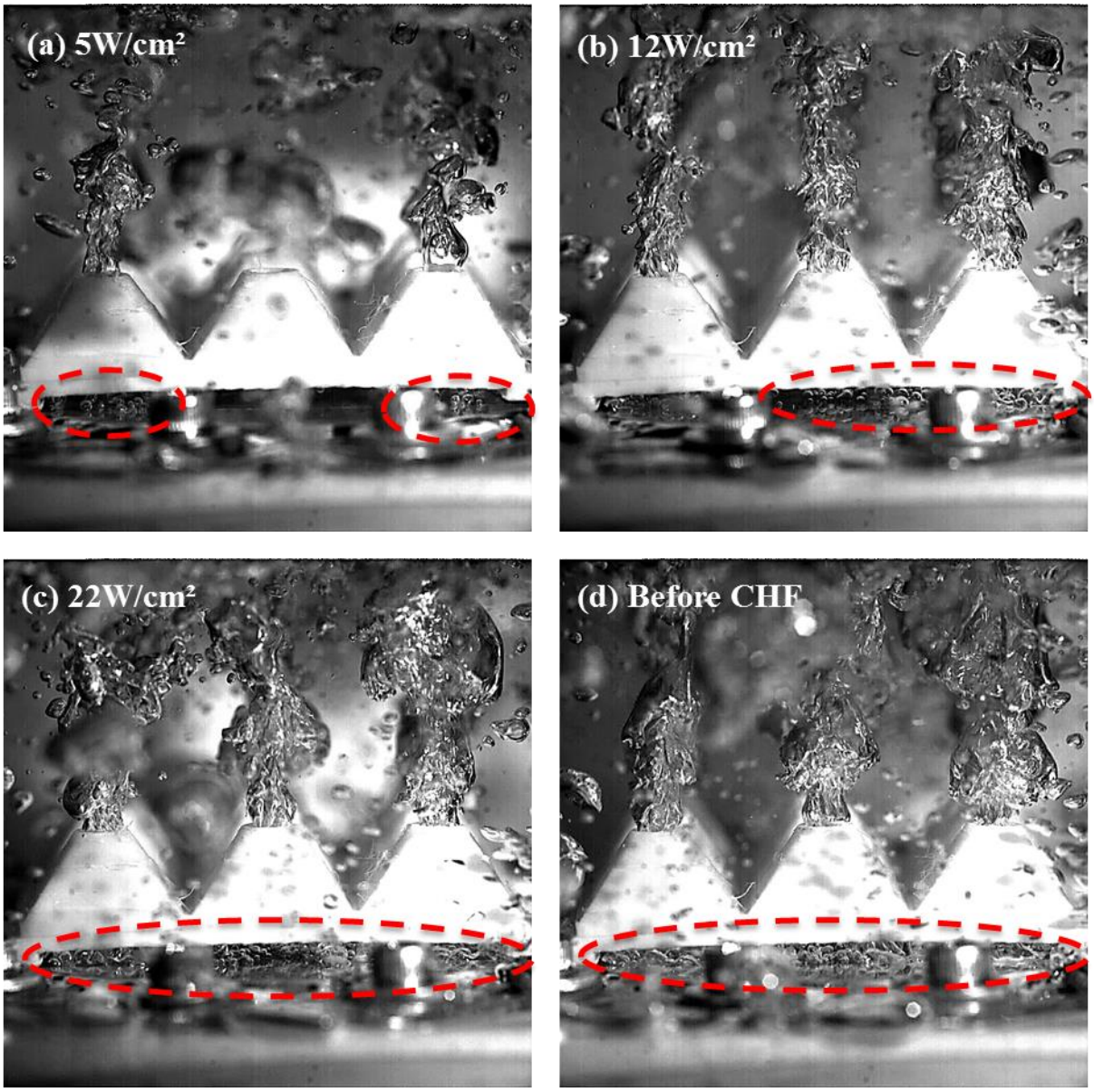

Figure 36. High-speed images of bubbles nucleation over plain chip using volcano manifold with increasing heat flux.

Figure 36 shows high-speed images of nucleation of bubbles (marked with dotted red circles) over the heater surface with volcano manifold at different heat fluxes. It is observed that bubbles exit through the top hole of HCS due to buoyancy force and the working fluid flows under the volcano manifold through the sides having a 1 mm gap. With high speed images, it is validated that the vapor does not escape from the sides but only from the top holes at both low and high heat fluxes. Thus, the volcano manifold can be used to create separate liquid vapor pathways on the heater surface without any deposition and/or chemical surface modification of the heater surface. By providing a gap between the volcano manifold and the

heater surface, the inertia force of incoming liquid increases and increases in velocity of liquid at the inlet is achieved. Additionally, the rewetting holes from the top of the volcano manifold act as impingement jets and help in reducing the wall superheat temperature.

6.3.2 Microchannel chip with volcano manifold

It was observed that PP1, PP1C and FC-87 obtained CHF at 32.1 W/cm², 37.2 W/cm², 33.2 W/cm², and heat transfer coefficients of 7.1 kW/m² °C, 7.3 kW/m² °C and 6.4 kW/m² °C, respectively. There is a noticeable increase in the wall superheat for a microchannel chip with volcano mnaifold, compared to a microchannel chip for all three refrigerants. Microchannel chips with the volcano manifold did not show any enhancement in CHF or HTC.

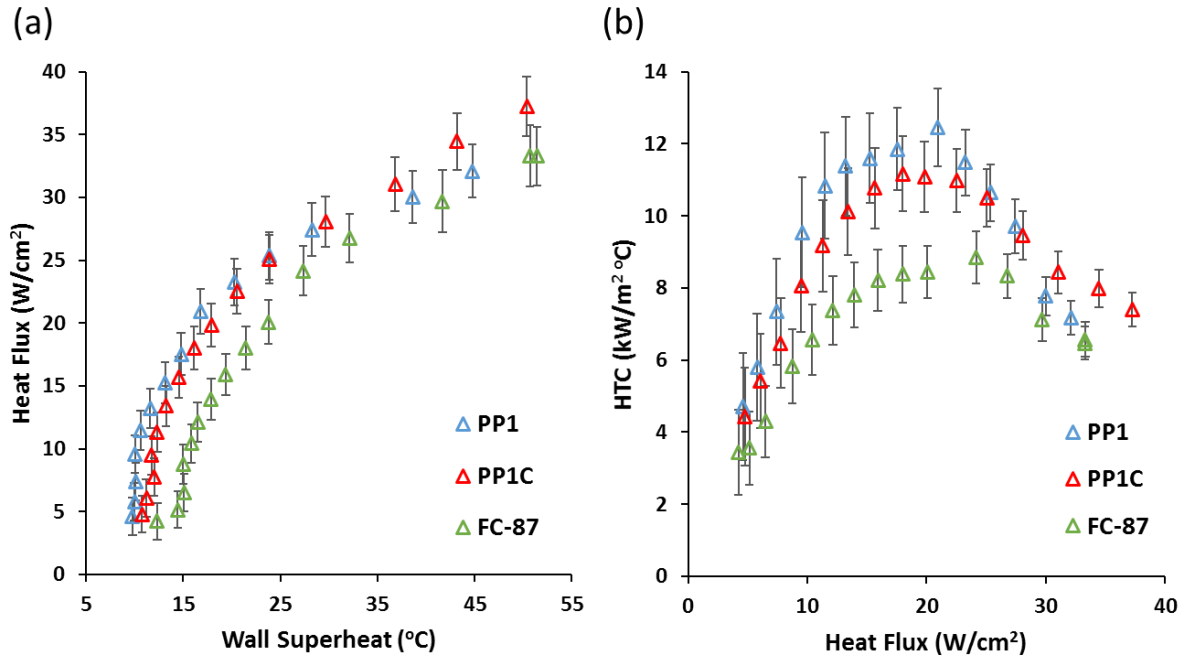

Figure 37. (a) Pool boiling curve and (b) HTC for tested refrigerants with microchannel chip and volcano manifold with rewetting holes of 1 mm diameter.

Microchannels with the volcano manifold follows a similar trend observed in a plain copper chip of decrease in HTC before reaching CHF. As shown in Figure 39 (b) there is a considerable drop in HTC after a heat flux of 20 W/cm² for all three refrigerants. At 20 W/cm²,

a HTC of 12.4 kW/m² °C, 11.0 kW/m² °C and 8.4 kW/m² °C was achieved for PP1, PP1C and FC-87, respectively (as shown in Fig. 39 b)).

6.4 Dual Taper Manifold

Figure 40 shows the dual taper geometry used during this study. The top surface of the dual taper manifold consists of 3 slots. Two slots serve the purpose of liquid inlet, whereas the middle slot serves the purpose of vapor removal. The liquid inlet slots and vapor removal slots are 1 mm x 34.5 mm and 1.5 mm x 34.5 mm, respectively. The bubble departure diameter for PP1 and PP1C are 1.56 mm and 1.37 mm, respectively [30]. The dimension for the liquid inlet slot is governed by bubble departure diameter of all three refrigerants. Thus, to avoid removal of vapors through the liquid inlet, the liquid inlet slot is 1 mm wide. Figure 40 shows the dual taper manifold used in this study. The main objective of using the dual taper manifold is to study the performance of an add-on enhancement structure over the heater surface that would direct the bulk liquid to the heater surface through a specific structure and achieve specific vapor removal pathway.

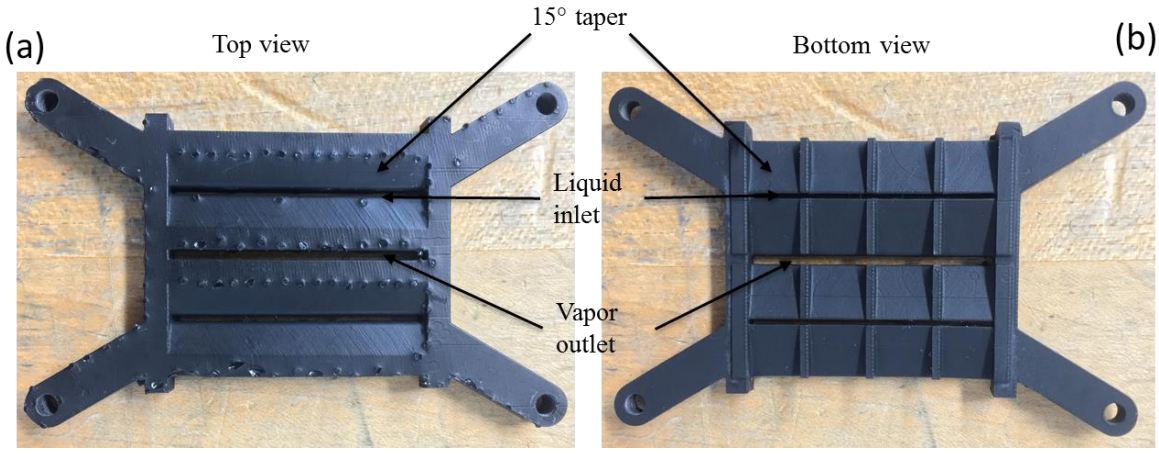

Figure 38. Actual image of dual taper 15°, (a) Top view and (b) Bottom view.

6.4.1 Plain copper chip with dual taper manifold

A plain copper chip was tested with the dual taper manifold of 15° and working fluids of PP1, PP1C and FC-87 at atmospheric pressure. It was observed that PP1, PP1C and FC-87 obtained

CHF of 25.6 W/cm², 31.7 W/cm² and 32.3 W/cm², respectively. While heat transfer coefficients of 7.2 kW/m² °C, 7.08 kW/m² °C and 6.7 kW/m² °C for PP1, PP1C and FC-87 for plain chip, respectively as shown in Figure 41 (b). It was observed that a very small increment in CHF was achieved for a plain chip with dual taper compared to a plain chip alone. However, a large increment in wall superheat was observed which led to reduced HTC. This increase in wall superheat is due to two reasons. Firstly, constricted flow due to 0.5 mm gap that did not allow adequate amount of liquid for rewetting of the surface. Secondly, the 0.5 mm gap between the dual taper manifold and the chip collapsed the vapor bubbles by lateral bubble expansion and restricting the bubbles to grow to their bubble departure diameter. Thus, it did not allow for efficient heat transfer and led to considerable increase in the wall superheat.

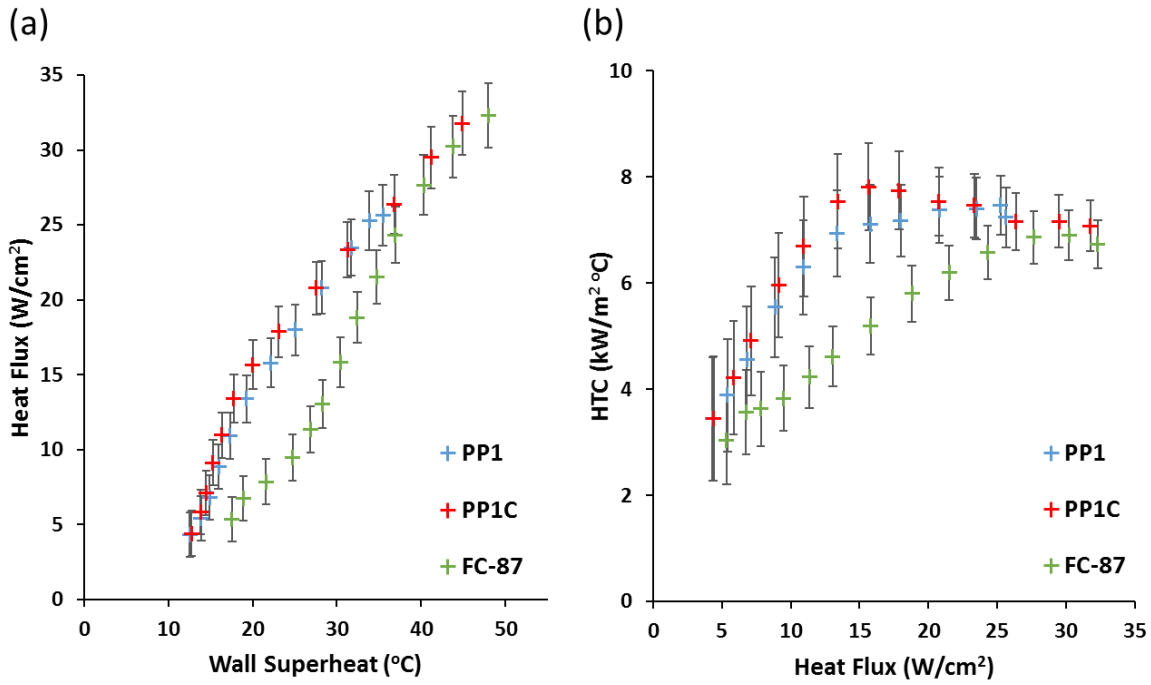

Figure 39. (a) Pool boiling curve and (b) HTC for tested refrigerants with plain chip and dual taper manifold of 15° taper angle.

Figure 42 shows a schematic representation of how the dual taper manifold regulates the flow of liquid over the heater surface through the 1 mm x 34.5 mm inlet slot. The taper at inlet reduces the resistance to the flow of liquid to the heater surface. The taper at the bottom surface directs the vapor bubbles generated to escape either from the center slot or from the sides.

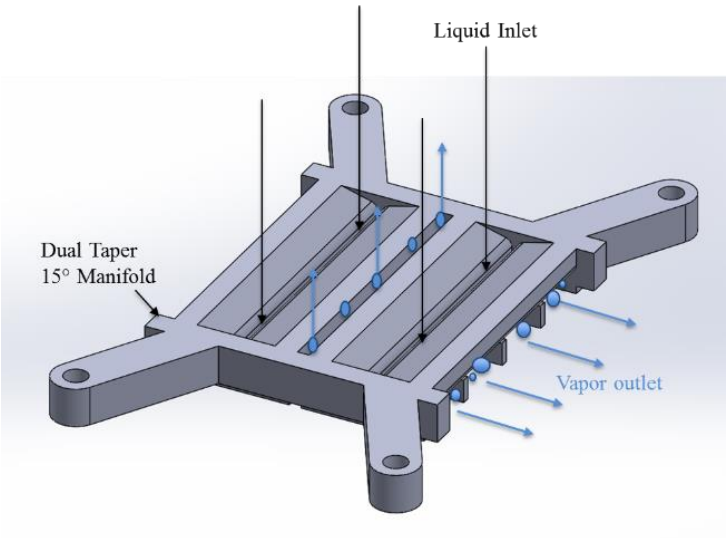

Figure 40. Schematic representation of separate liquid and vapor fields in Dual taper 15° manifold.

Figure 43 shows high-speed images of the vapor removal from a dual taper manifold with a 15° taper angle with plain copper chip and FC-87 at atmospheric pressure for 10 W/cm² and 22 W/cm². In Fig. 43 (a) and (c) the dashed red lines indicate the vapor escapes from the center slot of the dual taper manifold. Whereas in Figure 43(b) and (d) the dashed lines indicate vapor departing from the sides of the dual taper manifold. The increase in bubble nucleation at higher heat fluxes resulted in chaotic motion near the center, which was difficult to capture. The number of bubbles nucleating and exiting from the dual taper sides made it challenging to view vapor fields generated at the center of the dual taper.

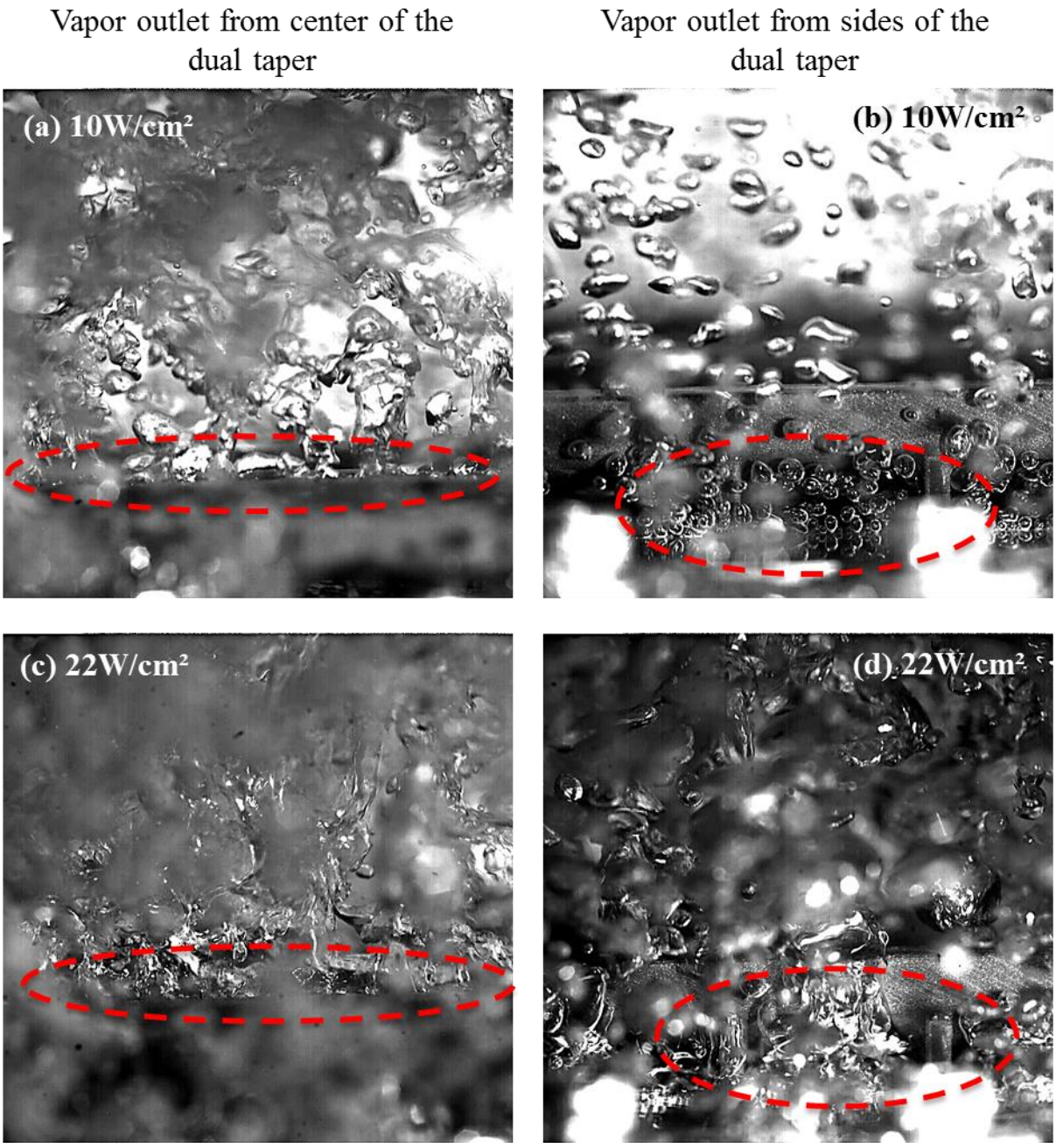

Figure 41. High-speed images of generated vapor pathway over plain chip with FC-87 at atmospheric pressure using dual taper manifold of 15° taper angle.

6.4.2 Microchannel chip with dual taper manifold

It was observed that PP1, PP1C and FC-87 obtained CHF at 35.5 W/cm², 36.9 W/cm², 36.7 W/cm², and heat transfer coefficient of 8.1 kW/m² °C, 7.3 kW/m² °C and 7.4 kW/m² °C, respectively. Compared to a microchannel chip with a volcano manifold, a microchannel chip with dual taper manifold of taper angle 15° showed a reasonable amount of increase in CHF

and HTC for PP1 and FC-87. A 10.9% and 10.5% increase in CHF was observed for PP1 and FC-87, respectively, compared to a microchannel chip with volcano manifold. It is suggested that the microchannel depth provided excess space to grow vapor bubbles in addition to the gap provided between the dual taper and the heater surface. These large vapor bubbles helped in dissipating more heat from the heater surface.

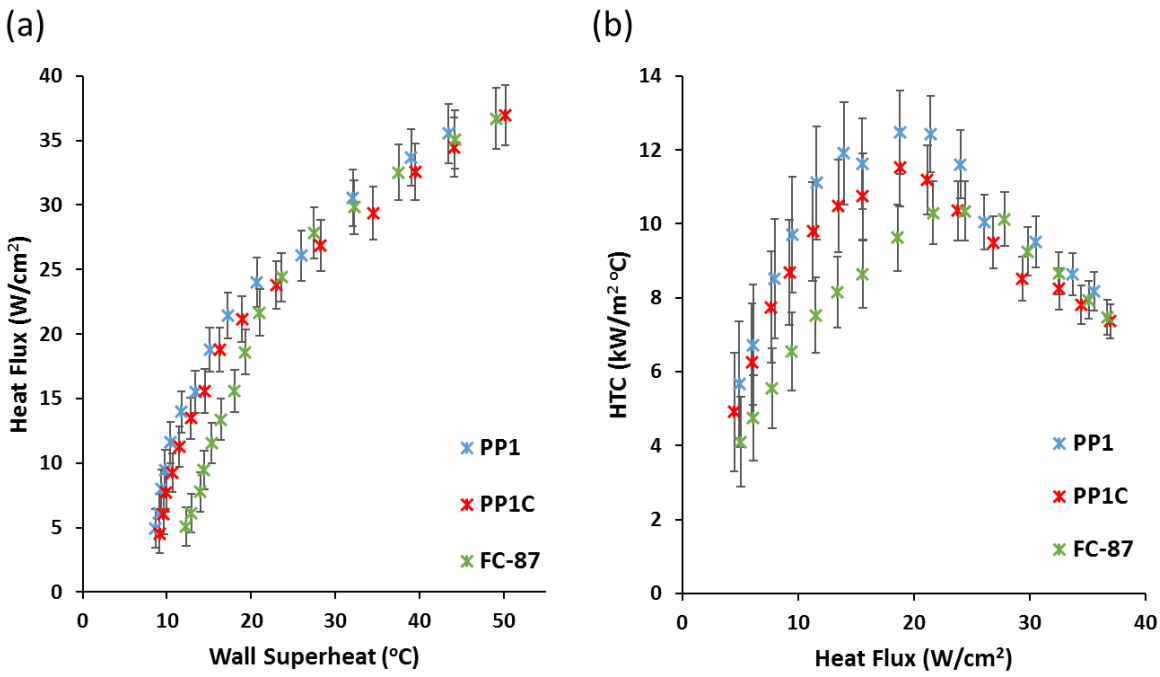

Figure 42. (a) Pool boiling curve and (b) HTC for tested refrigerants with microchannel chip and dual taper manifold of 15° taper angle.

As shown in Figure 44 (b) microchannels with dual taper manifold follow a similar trend observed in a plain chip and a microchannel chip with volcano manifold in Figure 36 and 39 shows a decrease in HTC before reaching CHF. Before HTC begins to drop with increase in heat flux at 20 W/cm², PP1 and PP1C achieve similar HTC with microchannel chip using volcano manifold. At 21 W/cm² FC-87 shows 21.4% increase in HTC (10.2 kW/m² °C) compared to microchannel with volcano manifold at the same heat flux.

6.5 Comparison of Larger Heater with Small Heater

In the current study, the plain copper chip used as the test section has a boiling surface of 34.5 mm x 32 mm referred to as the Large Heater or LH. Results from Chang et al. [31] for FC-87 and Emery et al. [13] for PP1 and PP1C have been plotted alongside the test performed in the current study for a plain copper chip using PP1, PP1C and FC-87 refrigerants at atmospheric pressure. Both authors use a polished plain copper test section of boiling surface 10 mm x 10 mm (referred as Small Heater or SH) for testing at atmospheric pressure.

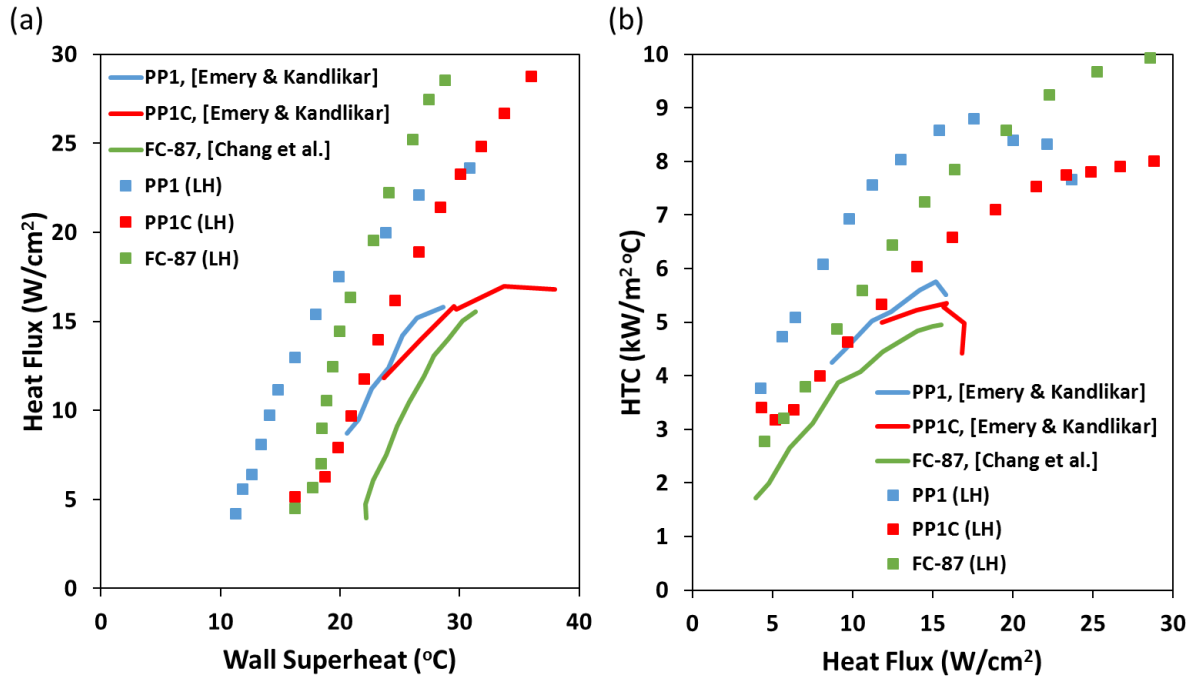

Figure 43. Comparison of pool boiling performance of larger heater with smaller heater for (a) the pool boiling curve and (b) HTC vs. heat flux.

In Figure 45(a) it is observed that the pool boiling curve for LH has shifted towards the left compared to the SH. For the same value of wall superheat, LH attains higher CHF values compared to SH for all three refrigerants. Similarly in Figure 45(b), for the same value of heat flux LH attains higher HTC compared to SH. The decrease in wall superheat and increase in heat flux for LH can be explained by Figure 46. Figure 46(a) shows the high-speed image of flow structure of liquid and vapor over a plain copper chip (LH) with working fluid as PP1 at

atmospheric pressure. The increase in performance for a LH can be accounted by the flow structure of the vapor. Bubbles coalesce and create vapor columns. With an increase in heat flux, these vapor columns coalesce and create a single plume or flower structure of vapor bubbles (as shown in Fig. 46(a)). This sets up the macro-convection currents due to which the liquid rush toward the heater surface from the sides of the plume. This enables the enhancement in both heat flux and heat transfer coefficients. Whereas, in Fig. 46(b) which shows the high-speed image of pool boiling for a SH, it is observed that at 18.5 W/cm², the bubble coalescence take place on a SH without the formation of any plume of vapour bubbles or flower type structure. Thus, these large convection currents are responsible for enhancing the performance of the LH as compared to the SH.

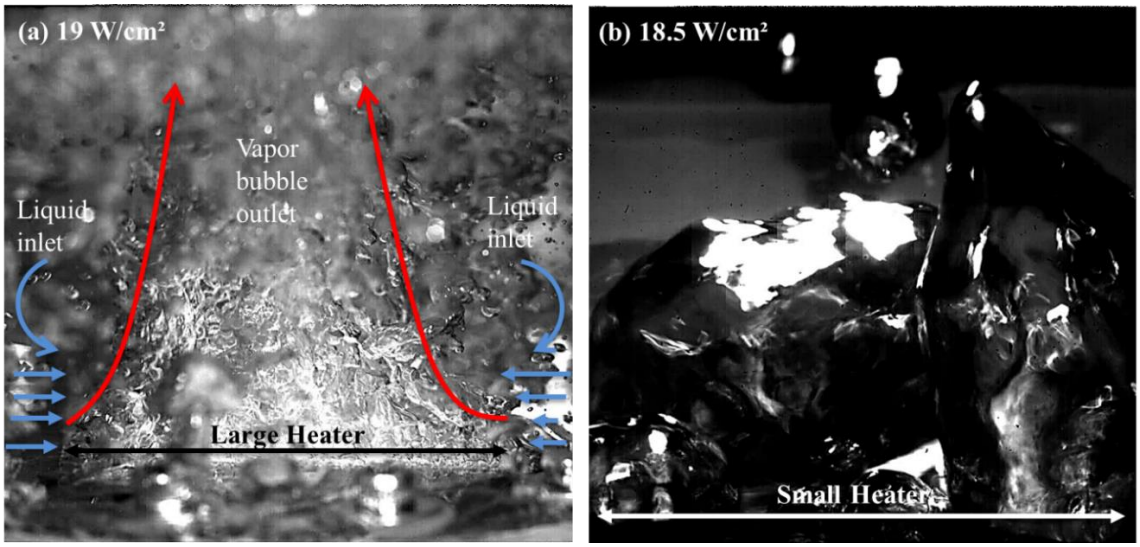

Figure 44. (a) pool boiling over larger heater at 19 W/cm² and (b) pool boiling over smaller heater at 18.5 W/cm².

Table 3 shows the results of CHF, wall superheat, and HTC for both smaller and larger heater. There is 31.03%, 66.6% and 104% increment in maximum heat transfer coefficient for PP1, PP1C and FC-87 with LH over SH at CHF.

Table 3. Pool boiling performance of smaller and larger heater.

Refrigerant and heater surface tested	CHF (W/cm²)	Wall superheat (°C)	HTC (kW/m² °C)
PP1[Smaller Heater] [13]	15.6	28.6	5.8
PP1C[Smaller Heater] [13]	16	37.5	4.8
FC-87[Smaller Heater] [32]	16	31.1	4.9
PP1 [Larger Heater]	23.6	30.8	7.6
PP1C [Larger Heater]	28.7	35.9	8.0
FC-87 [Larger Heater]	30.5	30.2	10.0

Table 4 shows the comparison of CHF and HTC for experiments conducted on plain chip and plain chip with volcano and dual taper manifold. Plain copper chip with both volcano and dual taper manifold outperforms plain chip in CHF. Thus, suggesting that add-on enhancement structures help in delaying the CHF by regulating the flow of vapor through specific structures and providing continuous supply of liquid to the heater surface.

Table 4. CHF and HTC for experiments conducted on plain chip and plain chip with volcano and dual taper manifold.

Test chips	PP1		PP1C		FC-87	
	CHF (W/cm²)	HTC (kW/m² °C)	CHF (W/cm²)	HTC (kW/m² °C)	CHF (W/cm²)	HTC (kW/m² °C)
Plain chip	23.6	7.6	28.7	8.0	30.5	10.0
Plain chip with volcano manifold	28.1	8.8	38.3	7.8	32.5	8.7
Plain chip with dual taper	25.6	7.2	31.7	7.08	32.3	6.7

7. Conclusions

In the present study, three refrigerants, perfluoro-2methylpentane (PP1), perfluoro-methyl-cyclopentane (PP1C) and fluorocarbon (FC-87) have been tested for their pool boiling performance at an atmospheric pressure with boiling test section of 34.5 mm x 32 mm in a closed loop pool boiling setup. The study also explores two configuration: 1) Volcano Manifold and 2) Dual Taper Manifold as add-on enhancement structures over the heater surface without any deposition and/or chemical surface modification to the heater surface. These enhancement structures were created using an additive manufacturing technique to develop a unidirectional flow of liquid and vapor fields over the heater surface. High-speed images suggest that both the volcano manifold and dual taper manifold achieved high heat flux dissipation by regulating vapor removal and liquid supply to the heater surface. The pool boiling performance for the plain copper chips and all the modifications is as follow:

- For a plain copper chip, critical heat flux of 23.6 W/cm^2, 28.7 W/cm^2 and 30.5 W/cm² were achieved at wall superheats of 30.8°C, 35.9°C and 30.2°C for PP1, PP1C and FC-87, respectively. The maximum heat transfer coefficients achieved were 7.6 kW/m² °C, 8.0 kW/m² °C, and 10.0 kW/m² °C.
- Microchannel chip with channel width 500 µm, channel depth 400 µm, and fin width 200 µm achieved maximum heat flux (without reaching CHF) of 42 W/cm², 40.6 W/cm² and 36.5 W/cm² at a wall superheat of 19.6°C, 26.4°C and 23.6°C for PP1, PP1C and FC-87, respectively. The maximum heat transfer coefficient achieved for the corresponding heat fluxes was 21.8 kW/m² °C, 15.3 kW/m² °C and 15.4 kW/m² ° C.
- In the configuration of plain chip with volcano manifold having rewetting holes of 1 mm diameter, CHF and HTC of 28.1 W/cm², 38.3 W/cm² and 32.5 W/cm² and 8.8 kW/m² °C, 7.8 kW/m² °C and 8.7 kW/m² °C for PP1, PP1C and FC-87 were achieved,

respectively. The gap provided between the volcano manifold and the heater surface facilitated in modulating the flow over the heater surface by creating separate liquid-vapor pathways.

- Small increment in CHF was achieved with plain chip and dual taper manifold of taper angle 15°, since a gap of 0.5 mm provided between the dual taper manifold and the heater surface collapsed the vapor bubbles before they grew to their bubble departure diameter. Thus, led to increase in wall superheat and inefficient heat transfer from the heater surface.
- Add-on enhancement structures did not show improvement with microchannel chips. The gap provided between the heater surface, the manifold and taper angles need further optimization in order to obtain better heat transfer performance with microchannel chip.
- By using all the three refrigerants, the large heater (34.5 mm x 32 mm) performed better than the small heater (10 mm x 10 mm) by giving higher CHF and HTC. Flow structure of the vapor accounted for this increase in performance. High-speed images suggested that single plume or flower structure of vapor bubbles is created over the larger heater. This flow structure creates a macro-convection current due to which liquid rush towards the heater surface from the sides of the plume.

8. Recommendations for Future Work

- The current study conducts experiments on taper angle 15° and gap 0.5 mm. A parametric study can be conducted on taper angle and gap required between the dual taper manifold and the heater surface. A new dual taper manifold is proposed with taper angles of 5° and 10° with different gaps of 0.5 mm, 1 mm and 1.5 mm to obtain the relation between these parameters and their effect on heat flux and wall superheat temperature.

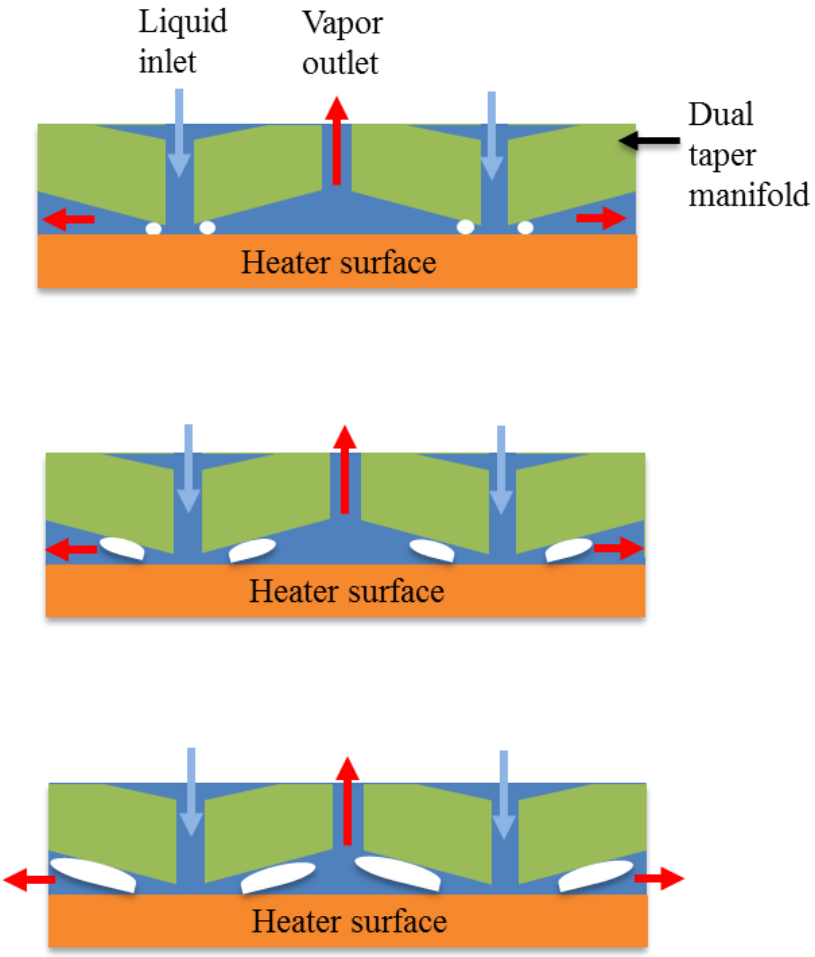

Figure 45. Expected bubble behaviour in dual taper manifold.

- The heater surface for the current study is developed to match the geometry of actual CPU surface dimensions. Experiments performed on a plain copper chip with three

dielectric fluids provides baseline results for heat transfer dissipated from a 34.5 mm x 32 mm heater surface. It also provides a direct comparison of heat transfer performance with an air cooled CPU surface.

- The current study uses a 3x3 array of hollow conical structures with base length of 9.75 mm, top hole diameter of 3 mm and height 5.75 mm. A new volcano manifold can be designed with 2 x 2 array of HCS and different base length, top hole and height parameters. Another parameter such as the gap provided between the volcano manifold and heater surface can be changed from 1 mm to 0.5 mm, 1.5 mm and 2 mm for further understanding the effect on the pool boiling performance.
- A more detailed parametric study needs to be conducted to obtain geometries that are able to enhance the performance significantly.
- Theoretical modelling of these structures is recommended. It is proposed that theoretical model of these enhancement structures can be created in ANSYS to further understand how the change in parameters such as microgap between the heater surface and the manifold, taper angles, and array of hollow conical structures affect the overall pool boiling performance.

9. References

[1] Walunj, A., and Sathyabhama, A., 2019, "Bubble Dynamics and Enhanced Heat Transfer During High-Pressure Pool Boiling on Rough Surface," J. Thermophys. Heat Transf., **33**(2), pp. 309–321.

[2] Chang, J. Y., and You, S. M., 1997, "Boiling Heat Transfer Phenomena from Microporous and Porous Surfaces in Saturated FC-72," Int. J. Heat Mass Transf., **40**(18), pp. 4437–4447.

[3] Chan, M. A., Yap, C. R., and Ng, K. C., 2010, "Pool Boiling Heat Transfer of Water on Finned Surfaces at Near Vacuum Pressures," J. Heat Transf., **132**(3), p. 031501.

[4] Yao, Z., Lu, Y.-W., and Kandlikar, S. G., 2011, "Effects of Nanowire Height on Pool Boiling Performance of Water on Silicon Chips," Int. J. Therm. Sci., **50**(11), pp. 2084–2090.

[5] NUKIYAMAt, S., "AND MINIMUM VALUES OF THE HEAT Q FROM METAL TO BOILING WATER UNDER ATMOSPHERIC PRESSURE," p. 12.

[6] "Additive Manufacturing: Industry Trends and Outlook," Formlabs [Online]. Available: http://formlabs.com/blog/additive-manufacturing/. [Accessed: 08-Jun-2019].

[7] "The Ultimate Guide to Stereolithography (SLA) 3D Printing (Updated for 2019)," Formlabs [Online]. Available: http://formlabs.com/blog/ultimate-guide-to-stereolithography-sla-3d-printing/. [Accessed: 09-Jun-2019].

[8] 2017, "Types of 3D Printers: Complete Guide - SLA, DLP, FDM, SLS, SLM, EBM, LOM, BJ, MJ Printing," 3D Insid. [Online]. Available: https://3dinsider.com/3d-printer-types/. [Accessed: 09-Jun-2019].

[9] Chauhan, A., "CPU Cooling in Data Center Using a Thermosiphon Loop with Tapered Open Microchannel Manifold (OMM)," p. 95.

[10] Cooke, D., and Kandlikar, S. G., 2011, "Pool Boiling Heat Transfer and Bubble Dynamics Over Plain and Enhanced Microchannels," J. Heat Transf., **133**(5), p. 052902.

[11] Cooke, D., and Kandlikar, S. G., 2012, "Effect of Open Microchannel Geometry on Pool Boiling Enhancement," Int. J. Heat Mass Transf., **55**(4), pp. 1004–1013.

[12] Kalani, A., and Kandlikar, S. G., 2013, "Enhanced Pool Boiling With Ethanol at Subatmospheric Pressures for Electronics Cooling," J. Heat Transf., **135**(11), pp. 111002-111002–7.

[13] Emery, T. S., and Kandlikar, S. G., 2017, "Pool Boiling with Four Non-Ozone Depleting Refrigerants and Comparison with Previously Established Correlations," Exp. Therm. Fluid Sci., **85**(Supplement C), pp. 132–139.

[14] Jaikumar, A., and Kandlikar, S. G., 2015, "Enhanced Pool Boiling for Electronics Cooling Using Porous Fin Tops on Open Microchannels with FC-87," Appl. Therm. Eng., **91**, pp. 426–433.

[15] Rainey, K. N., and You, S. M., 2000, "Pool Boiling Heat Transfer From Plain and Microporous, Square Pin-Finned Surfaces in Saturated FC-72," J. Heat Transf., **122**(3), pp. 509–516.

[16] Jaikumar, A., and Kandlikar, S. G., 2016, "Ultra-High Pool Boiling Performance and Effect of Channel Width with Selectively Coated Open Microchannels," Int. J. Heat Mass Transf., **95**, pp. 795–805.

[17] Mahamudur Rahman, M., Pollack, J., and McCarthy, M., 2015, "Increasing Boiling Heat Transfer Using Low Conductivity Materials," Sci. Rep., **5**.

[18] Jaikumar, A., and Kandlikar, S. G., 2016, "Pool Boiling Enhancement through Bubble Induced Convective Liquid Flow in Feeder Microchannels," Appl. Phys. Lett., **108**(4), p. 041604.

[19] Hayes, A., Raghupathi, P. A., Emery, T. S., and Kandlikar, S. G., 2019, "Regulating Flow of Vapor to Enhance Pool Boiling," Appl. Therm. Eng., **149**, pp. 1044–1051.

[20] Kwark, S. M., Amaya, M., Kumar, R., Moreno, G., and You, S. M., 2010, "Effects of Pressure, Orientation, and Heater Size on Pool Boiling of Water with Nanocoated Heaters," Int. J. Heat Mass Transf., **53**(23), pp. 5199–5208.

[21] Rainey, K. N., and You, S. M., 2001, "Effects of Heater Size and Orientation on Pool Boiling Heat Transfer from Microporous Coated Surfaces," Int. J. Heat Mass Transf., **44**(14), pp. 2589–2599.

[22] Rainey, K. N., and You, S. M., 2001, "E€ ects of Heater Size and Orientation on Pool Boiling Heat Transfer from Microporous Coated Surfaces," Int. J. Heat Mass Transf., p. 11.

[23] "'Iridescent Ice' Clear Translucent HTPLA," ProtoPlant Mak. Proto-Pasta [Online]. Available: https://www.proto-pasta.com/products/high-temp-pla-v2-0. [Accessed: 26-Jun-2019].

[24] "Form Cure Time and Temperature Settings" [Online]. Available: https://support.formlabs.com/s/article/Form-Cure-Time-and-Temperature-Settings?language=en_US. [Accessed: 29-Jul-2019].

[25] Emery, T. S., Cliauhan, A., Plato, E. D., and Kandlikar, S. G., 2017, "CPU Cooling with a Thermosiphon Loop with Tapered Manifold (OMM)," *2017 16th IEEE Intersociety Conference on Thermal and Thermomechanical Phenomena in Electronic Systems (ITherm)*, pp. 864–870.

[26] Panse, S. S., and Kandlikar, S. G., 2017, "A Thermosiphon Loop for High Heat Flux Removal Using Flow Boiling of Ethanol in OMM with Taper," Int. J. Heat Mass Transf., **106**, pp. 546–557.

[27] Rego, P. K. B., “Flow Boiling in Open Microchannels with Tapered Manifolds Using Ethanol in a Gravity-Driven Flow,” p. 91.

[28] Patil, C. M., Santhanam, K. S. V., and Kandlikar, S. G., 2014, “Development of a Two-Step Electrodeposition Process for Enhancing Pool Boiling,” Int. J. Heat Mass Transf., **79**, pp. 989–1001.

[29] Mori, S., and Okuyama, K., 2009, “Enhancement of the Critical Heat Flux in Saturated Pool Boiling Using Honeycomb Porous Media,” Int. J. Multiph. Flow, **35**(10), pp. 946–951.

[30] Jaikumar, A., Emery, T. S., and Kandlikar, S. G., 2018, “Interplay between Developing Flow Length and Bubble Departure Diameter during Macroconvection Enhanced Pool Boiling,” Appl. Phys. Lett., **112**(7), p. 071603.

[31] Chang, J. Y., You, S. M., and Haji-Sheikh, A., 1998, “Film Boiling Incipience at the Departure From Natural Convection on Flat, Smooth Surfaces,” J. Heat Transf., **120**(2), p. 402.

Appendix

Validation of Fourier's Law of 1-D conduction

In section 4, we measure the heat flux through the heater neck with the Fourier's law of 1-D conduction. A numerical study was performed in ANSYS 18.1 to validate the experimental results. The 3D heater block (of the actual dimensions) created in SolidWorks was imported in the ANSYS Workbench 18.1 design modeller. The boiling heat transfer was studied at the top surface. 380 W of power was applied through the four cartridge heaters inserted at the bottom of the heater block as shown in Figure 18. Experimentally, the maximum heat transfer coefficient was achieved for microchannel chip. Therefore, this particular data set with heat transfer coefficient of 16.74 W/m²-°C for microchannel chip with PP1C dielectric fluid is chosen. The heater base and sides were insulated with garolite, which was exposed to air at room temperature. Effective thermal resistance provided by the garolite and air was calculated for the heater base and sides and heat transfer coefficient of 4 W/m²-°C was applied to the surface exposed to air. Figure 46 shows the temperature distribution along the heater block.

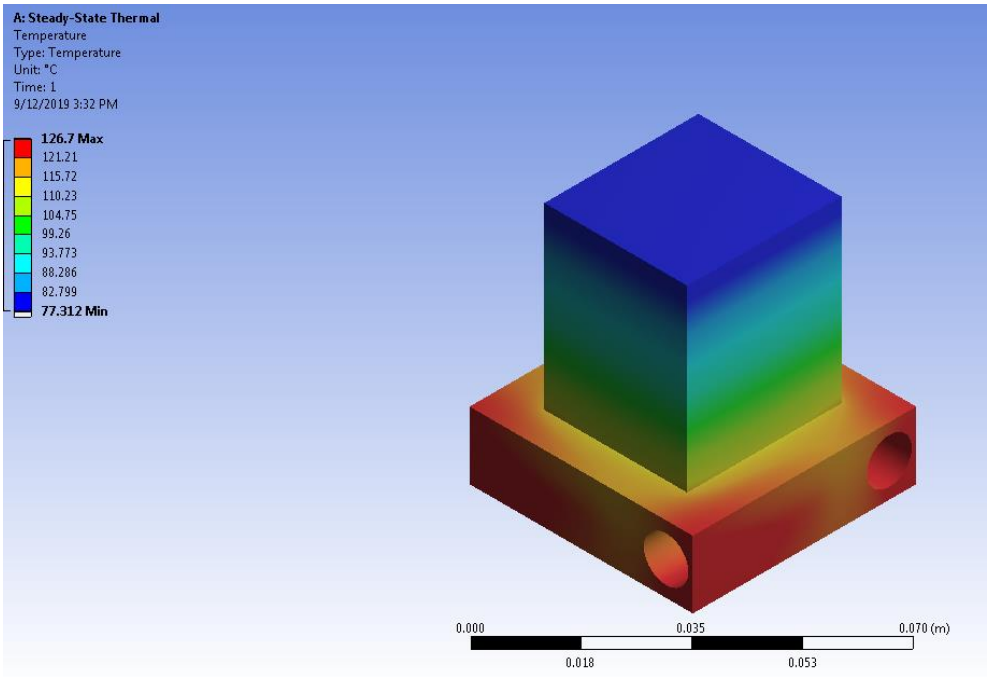

Figure 46 Temperature distribution along the heater block in ANSYS.

From the simulation, maximum temperature of 126 °C was achieved near the cartridge heaters and a minimum temperature of 77 °C at top surface of the heater block. As shown in Figure 18 there are three thermocouples inserted in the heater block to approximate the temperature gradient and calculate heat flux through the heater neck. Temperature for these three locations T_1, T_2 and T_3 were also obtained from the simulation as 90.4°C, 86.1°C and 81.7°C respectively.

Table 5. The temperature comparison between experimental and numerical results at T1, T2 & T3.

Thermocouple	Computed Data (°C)	Experimental Data (°C)	Difference
T_3 (Bottom)	90.4	90.2	0.2
T_2 (Middle)	86.1	86.3	0.2
T_1 (Top)	81.7	82.1	0.4

The Table 5 shows the comparison between the temperatures at T_1, T_2 and T_3 from the numerical study and the experimental study. The difference between the experimental results and computed temperatures is less than 0.5°C, thus validating the experimental setup and showing that the heater follows the Fourier's law of 1-D conduction.

Heat loss study of the heating chip

In section 3.1, we introduced the heating chips and the heater assembly used in the current work. As shown in Figure 19, the test section is a 68 mm diameter copper chip with boiling surface of 34.5 mm x 32 mm at the center. Kapton tape was used to prevent heat transfer from the excess area. This tape has a low thermal conductivity of 0.12 W/m-K at 23°C. The garolite block was used to avoid heat losses from the heating chip. Garolite also has a low thermal conductivity of 0.2 W/m-K. A numerical study was performed in ANSYS 18.1 to investigate heat losses from the excess area covered by Kapton tape. Figure 47 shows the schematic representation of the heating chip with garolite block and the kapton tape insulation.

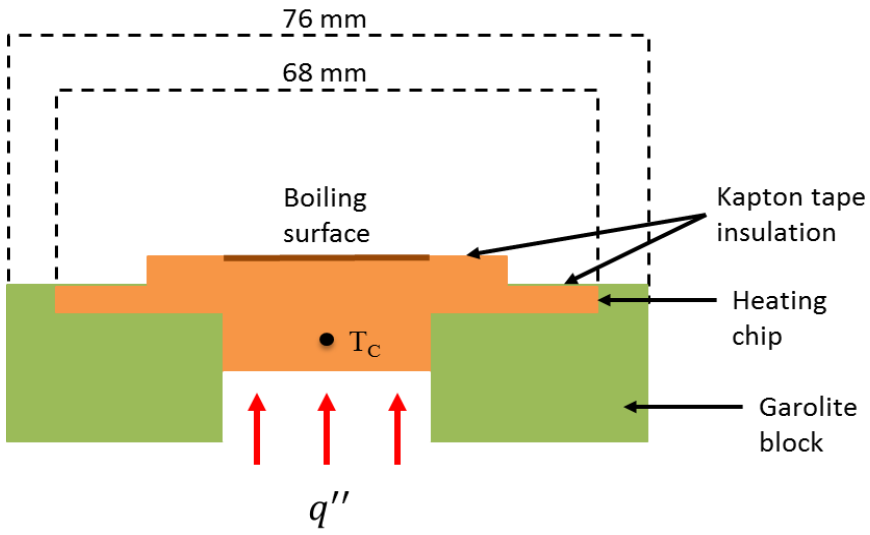

Figure 47. Schematic of heating chip.

The 3D microchannel chip created in SolidWorks was imported in the ANSYS Workbench 18.1 design modeller. Experimentally the maximum heat transfer coefficient was achieved for microchannel chip. Therefore, this particular data set with heat transfer coefficient of 16.74 kW/m² °C for microchannel chip with PP1C dielectric fluid was chosen. Figure 48 shows the boundary conditions over the heating chip. Convection on the top surface is due to boiling over the heater surface and thus the convective heat transfer coefficient of 16.74 kW/m² °C is applied (A). Effective thermal resistance provided by the Kapton tape was numerically calculated and

heat transfer coefficient of 0.384 W/m² °C was applied over the excess area of the top surface (B). The bottom surface of the chip, which consists of the thermocouple, T_C, is covered by garolite block on all four sides and hence the equivalent convective heat transfer coefficient due to air and garolite block was calculated as 5.71 W/m² °C and applied to the surfaces (C). The bottom surface of the heating chip was provided with 34.16 W/cm² heat flux calculated experimentally (D).

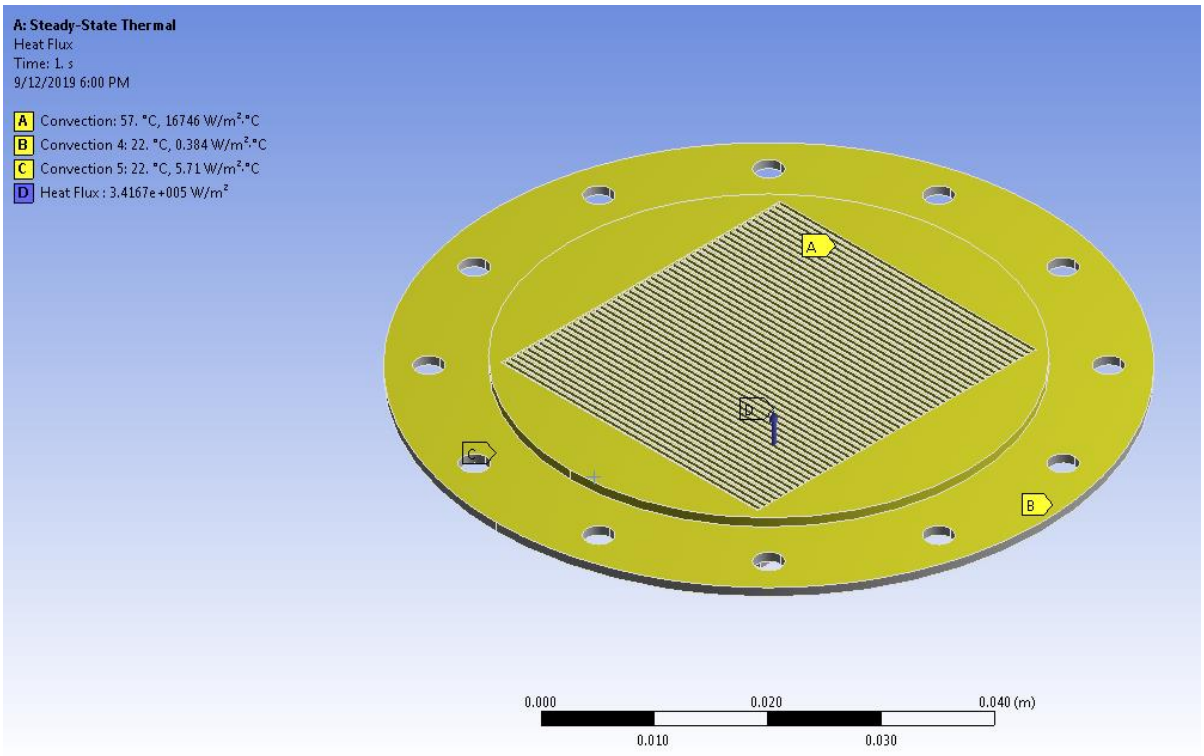

Figure 48. Boundary conditions.

Figure 49(a) shows the heat flux distribution over the heating chip. The excess area covered by the Kapton tape computed a heat flux dissipation of 0.0119W/cm² and shown as the blue region in Figure 49(a). Since the heat flux being dissipated by the boiling surface is much higher than the heat lost from the excess area, it is neglected. Figure 49(b) shows the temperature distribution over the heating chip. A maximum temperature of 73.3°C was achieved at the bottom of the heating chip and a minimum temperature of 67.7°C at the bottom surface of the

microchannels. The bottom surface of the microchannels have minimum temperature, as there is continuous heat removal from the surface due to boiling.

As shown in Figure 47 a thermocouple is inserted in the heating chip to calculate the surface temperature. Temperature for this location, T_C was also computed from the simulation as 73.3°C. Computed temperature at T_C from the simulation was compared with experimental study for the same location. Experimental study obtained 72.8°C for temperature at T_C, whereas simulation achieves 73.3°C at T_C. The difference between the experimental results and numerical study is 0.5°C. Thus, numerical study validates that a small amount of heat is being lost from the excess area and can neglected.

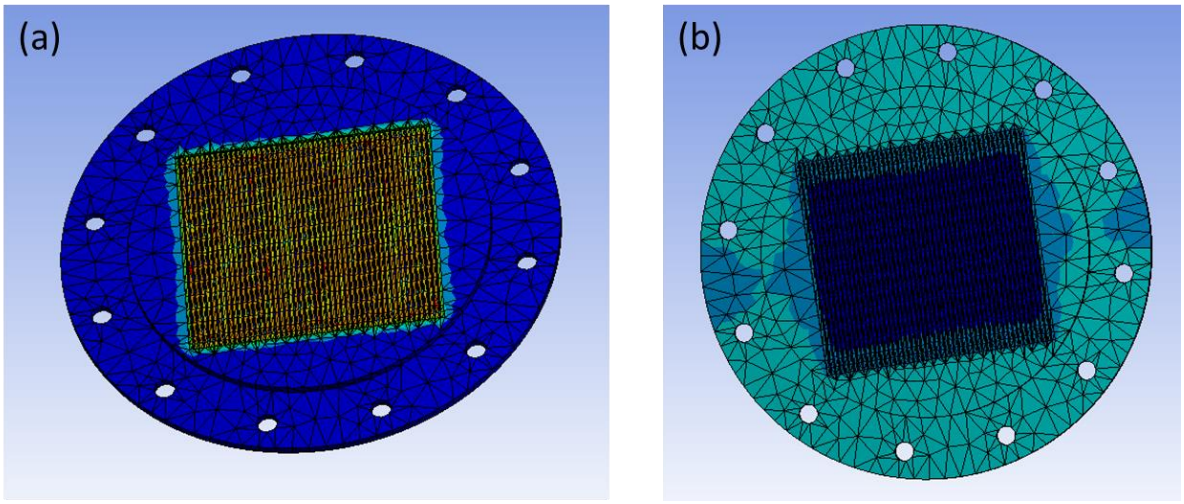

Figure 49. (a) Total heat flux and (b) Temperature distribution over the heating chip in ANSYS